

Cloud Retrieval Algorithms for MODIS: Optical Thickness, Effective Particle Radius, and Thermodynamic Phase

MICHAEL D. KING¹ AND SI-CHEE TSAY²
*NASA Goddard Space Flight Center
Greenbelt, Maryland 20771*

STEVEN E. PLATNICK² AND MENGHUA WANG²
*University of Maryland Baltimore County
NASA Goddard Space Flight Center
Greenbelt, Maryland 20771*

KUO-NAN LIOU
*Department of Meteorology
University of Utah
Salt Lake City, Utah 84112*

*MODIS Algorithm Theoretical Basis Document No. ATBD-MOD-05
MOD06 – Cloud product*

(3 October 1996, version 4)

¹Earth Sciences Directorate

²Laboratory for Atmospheres

TABLE OF CONTENTS

1. INTRODUCTION.....	1
2. OVERVIEW AND BACKGROUND INFORMATION.....	2
2.1. Experimental objectives.....	2
2.2. Historical perspective.....	5
2.3. Instrument characteristics.....	7
3. ALGORITHM DESCRIPTION	10
3.1. Theoretical description.....	10
3.1.1. Physics of problem.....	10
a. Cloud optical thickness and effective particle radius	10
b. Cloud thermodynamic phase.....	18
c. Ice cloud properties.....	20
3.1.2. Mathematical description of algorithm.....	22
a. Asymptotic theory for thick layers	22
b. Retrieval example.....	24
c. Atmospheric corrections: Rayleigh scattering.....	27
d. Atmospheric corrections: Water vapor.....	29
e. Technical outline of multichannel algorithm	31
f. Retrieval of cloud optical thickness and effective radius.....	36
3.2. Variance and uncertainty estimates	41
3.2.1. Model uncertainties.....	42
3.2.2. Physical uncertainties	49
3.3. Practical considerations.....	54
3.3.1. Numerical computation considerations.....	54

a. Parameter description.....	54
b. Data storage estimates.....	54
c. Data processing requirements	55
d. Required input data.....	56
e. Level-3 gridded data.....	57
3.3.2. Validation	58
3.3.3. Quality control, diagnostics, and exception handling	62
4. CONSTRAINTS, LIMITATIONS, AND ASSUMPTIONS.....	62
5. REFERENCES	63

1. Introduction

The intent of this document is to present algorithms for inferring certain optical and thermodynamical properties of cloud layers, specifically, optical thickness, effective particle radius, and particle phase from multiwavelength reflected solar and emitted thermal radiation measurements.

It is well known that clouds strongly modulate the energy balance of the Earth and its atmosphere through their interaction with solar and terrestrial radiation, as demonstrated both from satellite observations (Ramanathan 1987, Ramanathan et al. 1989) and from modeling studies (Ramanathan et al. 1983, Cess et al. 1989). However, clouds vary considerably in their horizontal and vertical extent (Stowe et al. 1989, Rossow et al. 1989), in part due to the circulation pattern of the atmosphere with its requisite updrafts and downdrafts, and in part due to the distribution of oceans and continents and their numerous and varied sources of cloud condensation nuclei (CCN). A knowledge of cloud properties and their variation in space and time, therefore, is crucial to studies of global climate change (e.g., trace gas greenhouse effects), as general circulation model (GCM) simulations indicate climate-induced changes in cloud amount and vertical structure (Wetherald and Manabe 1988), with a corresponding cloud feedback working to enhance global warming.

GCM simulations by Roeckner et al. (1987) and Mitchell et al. (1989) include corresponding changes in cloud water content and optical thickness, and suggest that changes in cloud optical properties may result in a negative feedback comparable in size to the positive feedback associated with changes in cloud cover. None of the GCM simulations to date include corresponding changes in cloud microphysical properties (e.g., particle size), which could easily modify conclusions thus far obtained. Of paramount importance to a comprehensive under-

standing of the Earth's climate and its response to anthropogenic and natural variability is a knowledge, on a global sense, of cloud properties that may be achieved through remote sensing and retrieval algorithms.

In this document we start with a background overview of the MODIS instrumentation and the cloud retrieval algorithms, followed by a description of the theoretical basis of the cloud retrieval algorithms to be applied to MODIS data. We follow with a discussion of practical considerations (including the constraints and limitations involved in the retrieval algorithms), outline our validation strategy, and present our plans for refinement of the algorithms during the pre-launch and post-launch development phases.

2. Overview and background information

The purpose of this document is to provide a description and discussion of the physical principles and practical considerations behind the remote sensing and retrieval algorithms for cloud properties that we are developing for MODIS. Since the development of the algorithms, to be used in analyzing data from the MODIS sensor system, is at the at-launch software development stage, this document is based on methods that have previously been developed for processing data from other sensors with similar spectral characteristics. Through continued interaction with the MODIS science team and external scientific community, we anticipate that these algorithms will be further refined for use in the processing of MODIS data, both through simulations and through airborne field experiments.

2.1. *Experimental objectives*

The main objective of this work is the development of routine and operational methods for simultaneously retrieving the cloud optical thickness and ef-

fective particle radius from daytime multiwavelength reflected solar and emitted thermal radiation measurements. Retrieval of cloud particle phase from visible and near-infrared solar reflection measurements will also be discussed. Methods presented here are based in part on the work of Nakajima and King (1990) and the review article of King et al. (1992), as well as on recent work utilizing the 3.7 μm channel of the Advanced Very High Resolution Radiometer (AVHRR) for the remote sensing of cloud optical and microphysical properties, described by Plattnick and Twomey (1994) and Nakajima and Nakajima (1995).

Figure 1 illustrates the data flow diagram for all of the MODIS atmosphere algorithms, including production of the cloud mask product (MOD35) and the MODIS cloud product (MOD06). Knowledge of particle phase, along with cloud cover, are necessary inputs for retrieving the cloud optical thickness and effective particle radius. Cloud cover will be provided by the cloud top properties algorithm of Menzel and Strabala (ATBD-MOD-04) based on analysis of the cloud mask algorithm of Ackerman et al. (ATBD-MOD-06). An algorithm for cloud particle phase, using emitted thermal radiation measurements, is also being developed by Menzel and Strabala (ATBD-MOD-04); our algorithm for thermodynamic phase complements theirs by adding reflected solar radiation measurements, and the two will eventually be included as separate parameters in the cloud product (MOD06).

The importance of retrieving the optical thickness and effective radius derives not only from the fact that such a retrieval is possible, but from the fact that shortwave cloud radiative properties depend almost exclusively on these two parameters. This thus forms the basis of cloud radiative parameterization methods, such as the one developed by Slingo (1989), which require that a global data base on the effective radius and optical thickness (or equivalently integrated liq-

uid water content) of clouds be available. Such data seem only to be derivable from spaceborne remote sensing observations. Therefore, MODIS is ideally suited to cloud remote sensing applications and retrieval purposes.

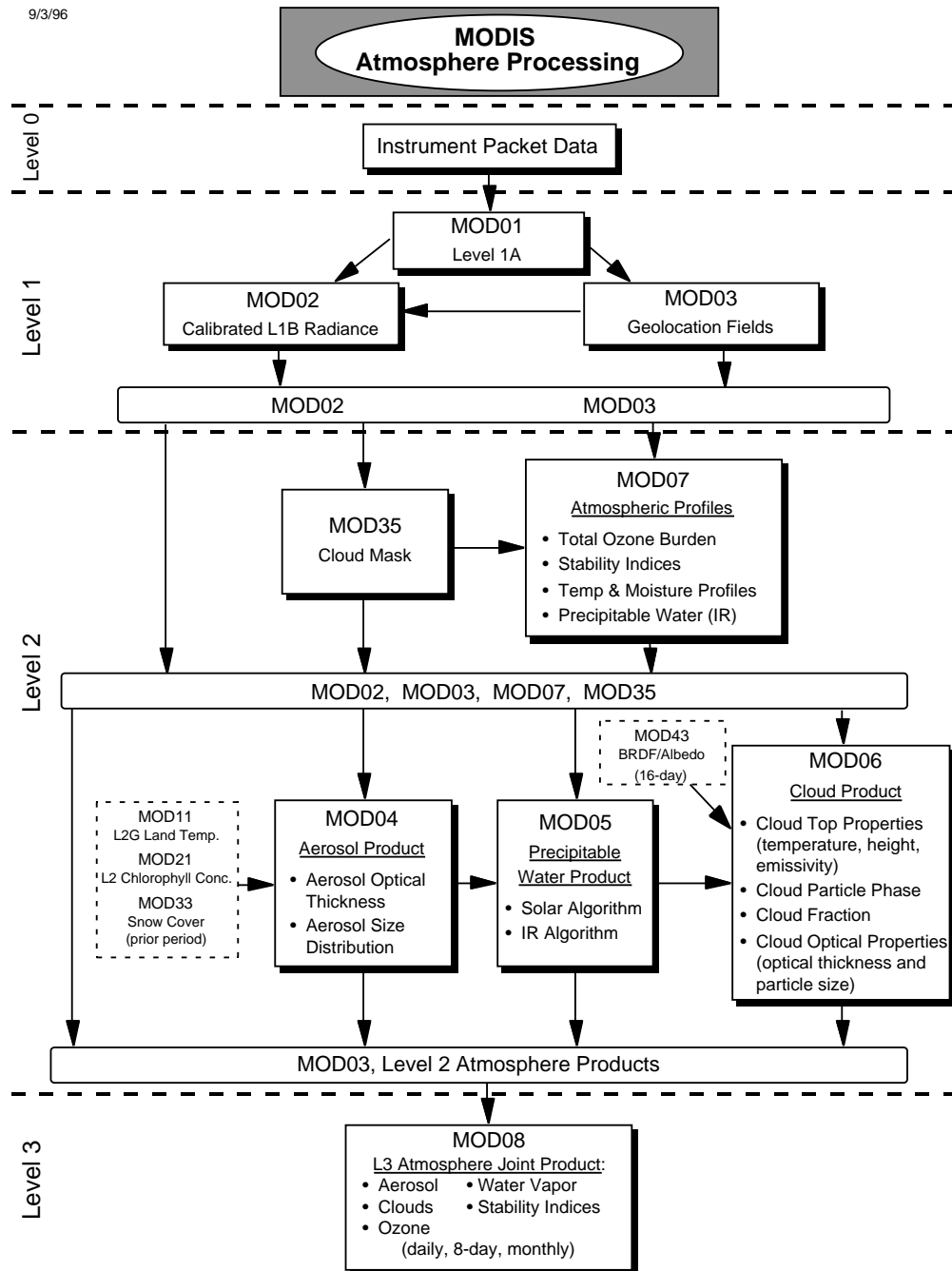


Figure 1. Data flow diagram for the MODIS atmosphere products, including product MOD06, some parameters of which (optical thickness and effective particle size) are produced by the algorithm described in this ATBD-MOD-06.

2.2. *Historical perspective*

Ever since the first launch of the TIROS-1 satellite in 1960, tremendous interest has arisen in the field of using these remotely sensed data to establish a global cloud climatology, in which a qualitative cloud atlas was archived. It has been a long-standing goal to quantify global cloud properties from spaceborne observations, such as cloud cover, cloud particle thermodynamic phase, cloud optical thickness and effective particle radius, and cloud top altitude and temperature. Many efforts in the past three decades (e.g., work dated as early as 1964 by Arking) have been devoted to extracting cloud cover parameters from satellite measurements.

There are a number of studies of the determination of cloud optical thickness and/or effective particle radius with visible and near-infrared radiometers on aircraft (Hansen and Pollack 1970, Twomey and Cocks 1982 and 1989, King 1987, Foot 1988, Rawlins and Foot 1990, Nakajima and King 1990, Nakajima et al. 1991) and on satellites (Curran and Wu 1982, Rossow et al. 1989). Further, the utility of the 3.7 μm channel onboard the AVHRR has been demonstrated by several investigators, including Arking and Childs (1985), Durkee (1989), Platnick and Twomey (1994), Han et al. (1994, 1995), Nakajima and Nakajima (1995) and Platnick and Valero (1995). The underlying principle on which these techniques are based is the fact that the reflection function of clouds at a nonabsorbing channel in the visible wavelength region is primarily a function of the cloud optical thickness, whereas the reflection function at a water (or ice) absorbing channel in the near-infrared is primarily a function of cloud particle size.

Twomey and Cocks (1989) developed a statistical method for simultaneously determining the cloud optical thickness and effective radius using reflected intensity measurements at several wavelengths in the near-infrared region. An

extension of this technique addresses the problem of identifying the thermodynamic phase of clouds (ice *vs* water) and of distinguishing clouds from snow surfaces by utilizing particular channels (e.g., 1.64 and 2.2 μm) which provide different absorption characteristics of water and ice (e.g., Pilewskie and Twomey 1987).

Although these studies have demonstrated the applicability of remote sensing methods to the determination of cloud optical and microphysical properties, more theoretical and experimental studies are required in order to assess the soundness and accuracy of these methods when applied to measurements on a global scale. From the theoretical point of view, the application of asymptotic theory to the determination of cloud optical thickness (King 1987) has demonstrated the physical basis of the optical thickness retrieval and its efficient implementation to experimental observations. This method is worth incorporating as one component of any multiwavelength algorithm for simultaneously determining the cloud particle phase, optical thickness and effective particle radius. From the experimental point of view, more aircraft validation experiments are required in order to assess the validity of these methods, since many factors affect the successful retrieval of these parameters when applied to real data in a real atmosphere (e.g., Rossow et al. 1985, Wu 1985).

Since 1986, an extensive series of field observations has been conducted. These include: FIRE-I/II Cirrus (First ISCCP Regional Experiment, 1986 and 1991, respectively), FIRE-I Stratocumulus (1987), ASTEX (Atlantic Stratocumulus Transition Experiment, 1992), TOGA/COARE (Tropical Ocean Global Atmosphere/Coupled Ocean-Atmosphere Response Experiment, 1993), CEPEX (Central-Equatorial Pacific Experiment, 1993), SCAR-A (Sulfate, Clouds And Radiation-Atlantic, 1993), MAST (Monterey Area Ship Track Experiment, 1994),

SCAR-C (Smoke, Clouds And Radiation - California, 1994), ARM-CAS (Arctic Radiation Measurements in Column Atmosphere-surface System, 1995), SCAR-B (Smoke, Clouds And Radiation - Brazil, 1995), and SUCCESS (Subsonic Aircraft Contrail and Cloud Effects Special Study, 1996). Instrumentation involved in these experiments has included either the MCR (Multispectral Cloud Radiometer; Curran et al. 1981) or MAS (MODIS Airborne Simulator; King et al. 1996), airborne sensors having spectral characteristics similar to a number of the cloud retrieval channels contained in MODIS, as well as the NOAA AVHRR satellite sensor. In the pre-launch stage of MODIS, these observational data, especially MAS data for which more than 500 research hours have thus far been obtained under various all-sky conditions, form the basis for our cloud retrieval algorithm development and validation.

2.3. *Instrument characteristics*

MODIS is a 36-channel scanning spectroradiometer. Four of these visible (0.645 μm) and near-infrared (1.64, 2.13, and 3.75 μm) spectral channels will be used in our daytime shortwave cloud retrieval algorithm over land surfaces, with 0.858 or 1.240 μm replacing 0.645 μm over ocean and bright snow/sea ice surfaces, respectively. Other channels in the thermal region, such as the 8.55, 11.03, 12.02, 13.335, 13.635, 13.935 and 14.235 μm channels, will be used for cloud cover and cloud top properties (including cloud top altitude, cloud top temperature and thermodynamic phase), as discussed elsewhere [Ackerman et al. (ATBD-MOD-06) and Menzel and Strabala (ATBD-MOD-04)]. In addition, the 11.03 μm channel will be used to make the thermal emission correction to the 3.75 μm channel during the day (see Section 3.1.2.c).

Figure 2 shows the wavelength locations of these primary MODIS shortwave

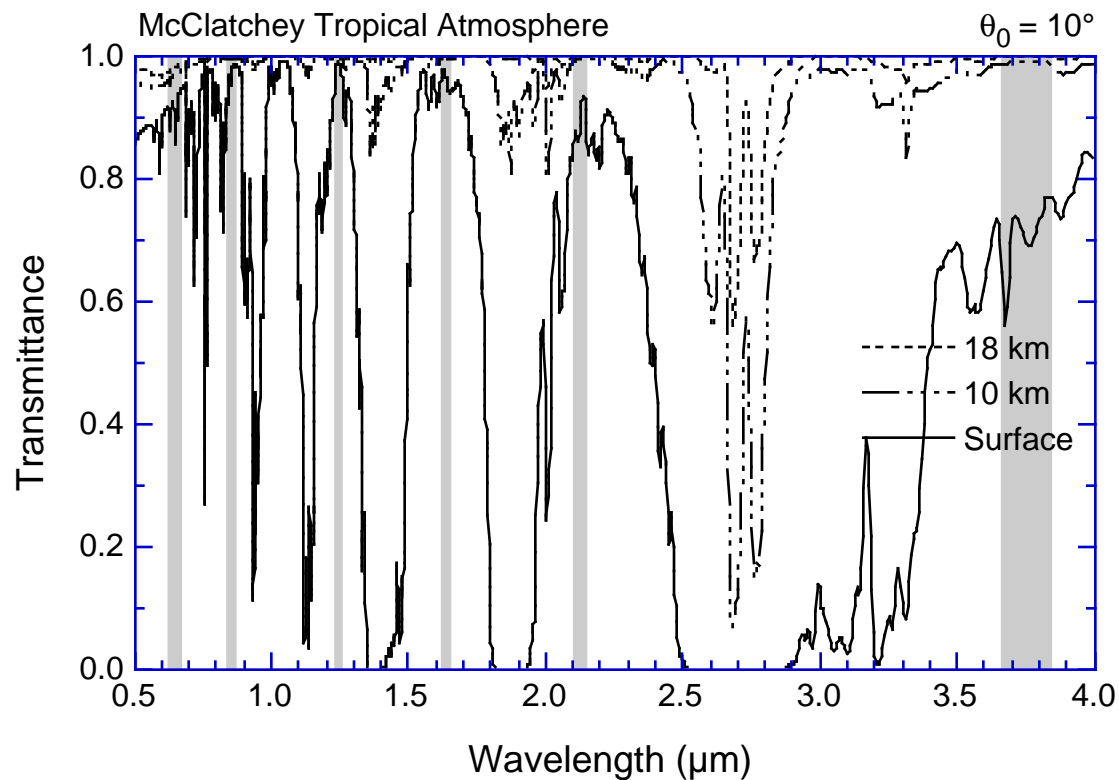


Figure 2. Spectral characteristics of six MODIS channels, centered at 0.65, 0.86, 1.24, 1.64, 2.13, and 3.75 μm , used for cloud property detection. The atmospheric transmittances are calculated from LOWTRAN 7 at 18 km, 10 km and at the surface for the McClatchey tropical atmosphere at 10° solar zenith angle.

channels, located in the water vapor window regions. The band center and bandwidth characteristics, as well as the dynamic range and main purpose(s) of each channel, are also summarized in Table 1. The 0.645, 2.13 and 3.75 μm channels will be used to retrieve the cloud optical thickness and effective particle radius over land (with 0.645 μm replaced by 0.858 μm over oceans and 1.24 μm over snow and sea ice surfaces); a combination of the 0.645, 1.64, and possibly the 2.13 μm channels will be used for cloud thermodynamic phase determination.

MODIS is designed to scan through nadir in a plane perpendicular to the velocity vector of the spacecraft, with the maximum scan extending up to 55° on either side of nadir (110° aperture). At a nominal orbital altitude for the EOS AM-1 spacecraft of 705 km, this yields a swath width of 2330 km centered on the

Table 1. Spectral characteristics, spatial resolution, saturation reflection function (at $\theta_0 = 22.5^\circ$), saturation brightness temperature, and principal purposes of cloud channels used on MODIS.

Channel	λ (μm)	$\Delta\lambda$ (μm)	Ground resolution (m)	R_{max}	T_{max} (K)	Atmospheric Purpose
1	0.645	0.050	250	1.43		Cloud optical thickness over land
2	0.858	0.035	250	0.96		Cloud optical thickness over ocean
5	1.240	0.020	500	0.78		Cloud optical thickness over snow & sea ice surfaces
6	1.640	0.025	500	1.02		Snow/cloud discrimination; thermodynamic phase
7	2.130	0.050	500	0.81		Cloud effective radius
20	3.750	0.180	1000		335	Cloud effective radius; Cloud/surface temperature
31	11.030	0.500	1000		400	Thermal correction

satellite ground track. In the baseline concept, the Earth-emitted and reflected solar radiation is incident on a two-sided scan mirror that continually rotates about an axis aligned with the direction of flight. Following the scan mirror is a telescope and a sequence of three dichroic beam splitters that further subdivide the incoming radiation into four focal planes. The 3.75 μm channel uses a ten-element linear array detector for the 1000 m spatial resolution bands, a 20-element array for the 500 m bands at the 1.64 and 2.13 μm channels, and a 40-element array for the 250 m band at 0.645 μm . They are aligned parallel to one another such that a single scan of the scan mirror is imaged on the focal plane for a swath 10 km in the along-track direction and 2330 km in the cross-track direction. In this configuration, all channels within a single focal plane are simultaneously sampled and registered within 0.1 pixel, with registration errors of less than 0.2 pixels between focal planes. The signal-to-noise ratio ranges between 57 and 1100 at a solar zenith angle $\theta_0 = 70^\circ$, depending on channel, and is considerably larger than these values at the solar zenith angle and scene temperature typical of the EOS AM-1 orbit ($\theta_0 = 22.5^\circ$).

For the algorithms discussed below, the MODIS data processing system will execute a preprocessor that integrates the 250 and 500 m bands to produce an equivalent 1000 m band using the point spread function of the MODIS spectroradiometer. In this way, all algorithms that use multispectral combinations of channels will be operating at a uniform spatial resolution. The native higher resolution bands will be used only for process studies associated with validation campaigns associated with coincident cloud microphysical measurements (see Section 3.3.2).

3. Algorithm description

In this section we will concentrate mainly on discussing the algorithm for simultaneously retrieving daytime cloud optical thickness and effective particle radius from multiwavelength reflected solar radiation measurements. In addition to the usual table lookup approach, we will utilize interpolation and asymptotic theory to fulfill this task, where appropriate. This procedure is especially direct and efficient for optically thick layers, where asymptotic expressions for the reflection function are the most valid, but can be applied to the full range of optical thicknesses using interpolation of radiative transfer calculations.

3.1. Theoretical description

3.1.1. Physics of problem

a. Cloud optical thickness and effective particle radius

Strictly speaking, our algorithm is mainly intended for plane-parallel liquid water clouds. It is assumed that all MODIS data analyzed by our algorithm has been screened by the cloud mask of Ackerman et al. (ATBD-MOD-06) with additional information regarding particle phase from the algorithm of Menzel and Strabala (ATBD-MOD-04), one component of developing product MOD06, as

outlined in Figure 1.

To retrieve the cloud optical thickness and effective particle radius, a radiative transfer model is first used to compute the reflected intensity field. It is convenient to normalize the reflected intensity (radiance) $I^\lambda(0, -\mu, \phi)$ in terms of the incident solar flux $F_0(\lambda)$, such that the reflection function $R^\lambda(\tau_c; \mu, \mu_0, \phi)$ is defined by

$$R^\lambda(\tau_c; \mu, \mu_0, \phi) = \frac{\pi I^\lambda(0, -\mu, \phi)}{\mu_0 F_0(\lambda)}, \quad (1)$$

where τ_c is the total optical thickness of the atmosphere (or cloud), μ_0 the cosine of the solar zenith angle θ_0 , μ the absolute value of the cosine of the zenith angle θ , measured with respect to the positive τ direction, and ϕ the relative azimuth angle between the direction of propagation of the emerging radiation and the incident solar direction.

When the optical thickness of the atmosphere is sufficiently large, numerical results for the reflection function must agree with known asymptotic expressions for very thick layers (van de Hulst 1980). Numerical simulations as well as asymptotic theory show that the reflection properties of optically thick layers depend essentially on two parameters, the scaled optical thickness τ_c' and the similarity parameter s , defined by

$$\tau_c' = (1 - \omega_0 g) \tau_c, \quad (2)$$

$$s = \left(\frac{1 - \omega_0}{1 - \omega_0 g} \right)^{1/2}, \quad (3)$$

where g is the asymmetry factor and ω_0 the single scattering albedo of a small volume of cloud layer. In addition, the reflectance properties of the Earth-atmosphere system depend on the reflectance (albedo) of the underlying surface,

A_g . The similarity parameter, in turn, depends primarily on the effective particle radius, defined by (Hansen and Travis 1974)

$$r_e = \frac{\int_0^\infty r^3 n(r) dr}{\int_0^\infty r^2 n(r) dr}, \quad (4)$$

where $n(r)$ is the particle size distribution and r is the particle radius. In addition to τ_c' , s and A_g , the details of the single scattering phase function affect the directional reflectance of the cloud layer (King 1987).

Our assumption here is that the reflection function is not dependent on the exact nature of the cloud particle size distribution, depending primarily on the effective radius and to a lesser extent on the effective variance, as first suggested by Hansen and Travis (1974). Nakajima and King (1990) showed that the similarity parameter is virtually unaffected by the effective variance (or standard deviation) of the cloud particle size distribution, but the asymmetry parameter, and hence scaled optical thickness, is weakly affected by the detailed shape of the size distribution.

For a channel with a finite bandwidth, Eq. (1) must be integrated over wavelength and weighted by the band's spectral response $f(\lambda)$ as well as by the incoming solar flux $F_0(\lambda)$. Hence, we can rewrite Eq. (1) as

$$R(\tau_c; \mu, \mu_0, \phi) = \frac{\int_\lambda R^\lambda(\tau_c; \mu, \mu_0, \phi) f(\lambda) F_0(\lambda) d\lambda}{\int_\lambda f(\lambda) F_0(\lambda) d\lambda}. \quad (5)$$

Values of the reflection function must be stored at three geometrical angles (θ_0, θ, ϕ), i optical thicknesses (τ_c), j prescribed effective particle radii (r_e), and k surface albedos (A_g). This forms a rather large lookup table and potentially causes sorting and computational inefficiencies.

The determination of τ_c and r_e from spectral reflectance measurements con-

stitutes the *inverse* problem and is typically solved by comparing the measured reflectances with entries in a lookup table and searching for the combination of τ_c and r_e that gives the best fit (e.g., Twomey and Cocks 1982, 1989). An alternative approach was suggested by Nakajima and King (1990), who showed that by applying asymptotic theory of optically thick layers, computations of the reflection function for a given value of τ_c , r_e and A_g can be determined efficiently and accurately, thereby reducing the size of the lookup tables required, and hence enabling application of analytic inversion and interpolation methods. This in no way alters the results of the retrieval, but simply makes use of efficient interpolation to reduce the size of the lookup tables and enhances the physical insight of the retrieval.

Figure 3 illustrates the spherical albedo as a function of wavelength for water clouds containing various values of the effective radius. Since the spherical albedo represents a mean value of the reflection function over all solar and observational zenith and azimuth angles, the reflection function itself must have a similar sensitivity to particle size. These computations were performed using asymptotic theory for thick layers and the complex refractive indices of liquid water, and include the additional contribution of water vapor. These computations strictly apply to the case when $\tau_c(0.75 \mu\text{m}) = 16$ and $A_g = 0.0$, and properly allow for the optical thickness and asymmetry factor to vary with wavelength in accord with our expectations for clouds composed solely of liquid water and water vapor (cf. King et al. 1990 for details). Since the similarity parameter is nearly zero (conservative scattering) in the water vapor windows at wavelengths $\lambda \lesssim 1.0 \mu\text{m}$, the cloud optical thickness can be derived primarily from reflection function measurements in this wavelength region. Figure 3 also shows that the spherical albedo, and hence reflection function, is sensitive to particle size at

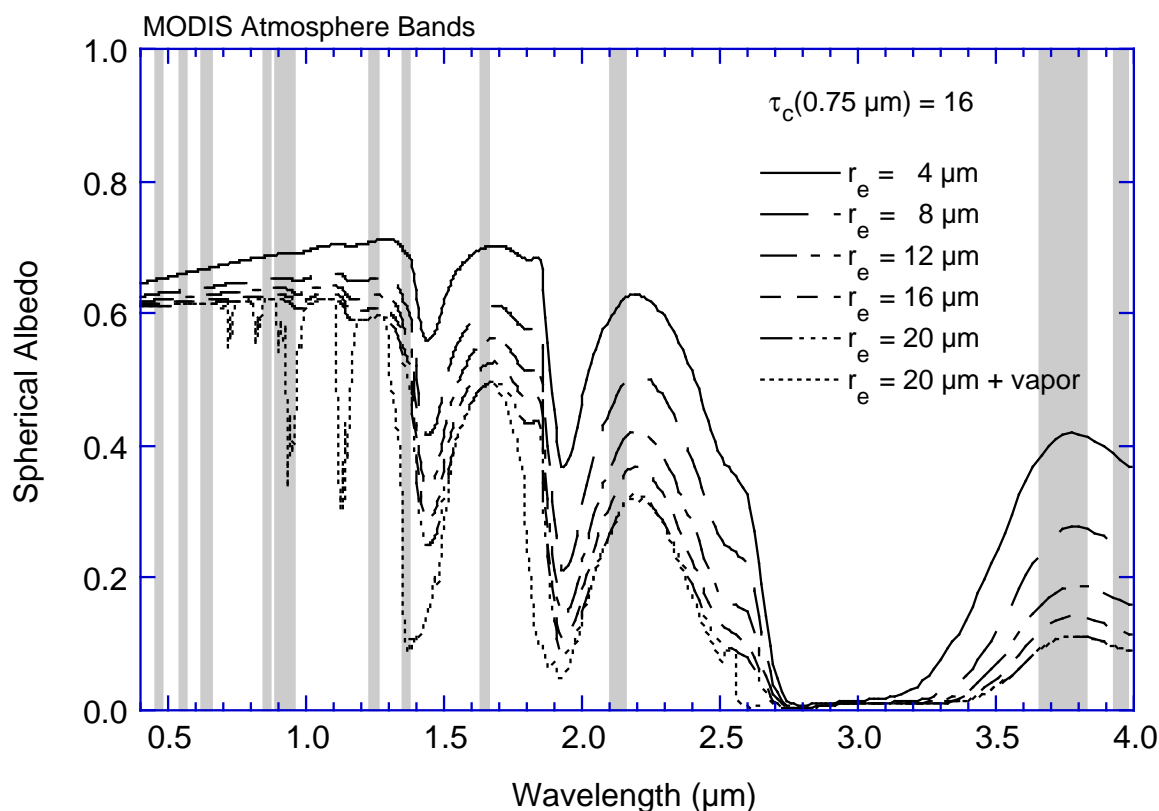


Figure 3. Cloud spherical albedo as a function of wavelength for selected values of the effective radius of cloud droplets. Results apply to water clouds having a modified gamma size distribution with an effective variance $v_e = 0.111$, cloud optical thickness $\tau_c(0.75 \mu\text{m}) = 16$, and saturated water vapor $w_g = 0.45 \text{ g cm}^{-2}$. The location and bandwidth of selected MODIS atmosphere bands are also shown in the figure.

wavelengths near 1.64, 2.13, and 3.75 μm , wavelengths for which water vapor absorption is small.

Cloud properties can also be estimated from the thermal bands. Figure 4 shows the top-of-the-atmosphere brightness temperature as a function of wavenumber (wavelength) from 600-3340 cm^{-1} (3-16.7 μm) for both clear and cloud sky conditions, where all computations were made using the discrete ordinates radiative transfer model developed by Tsay et al. (1990). These computations apply to mid-latitude summer conditions, an ocean-like surface having a temperature of 294 K, unit emissivity (zero reflectance), and overhead sun. These computations further include gaseous absorption (water vapor, carbon di-

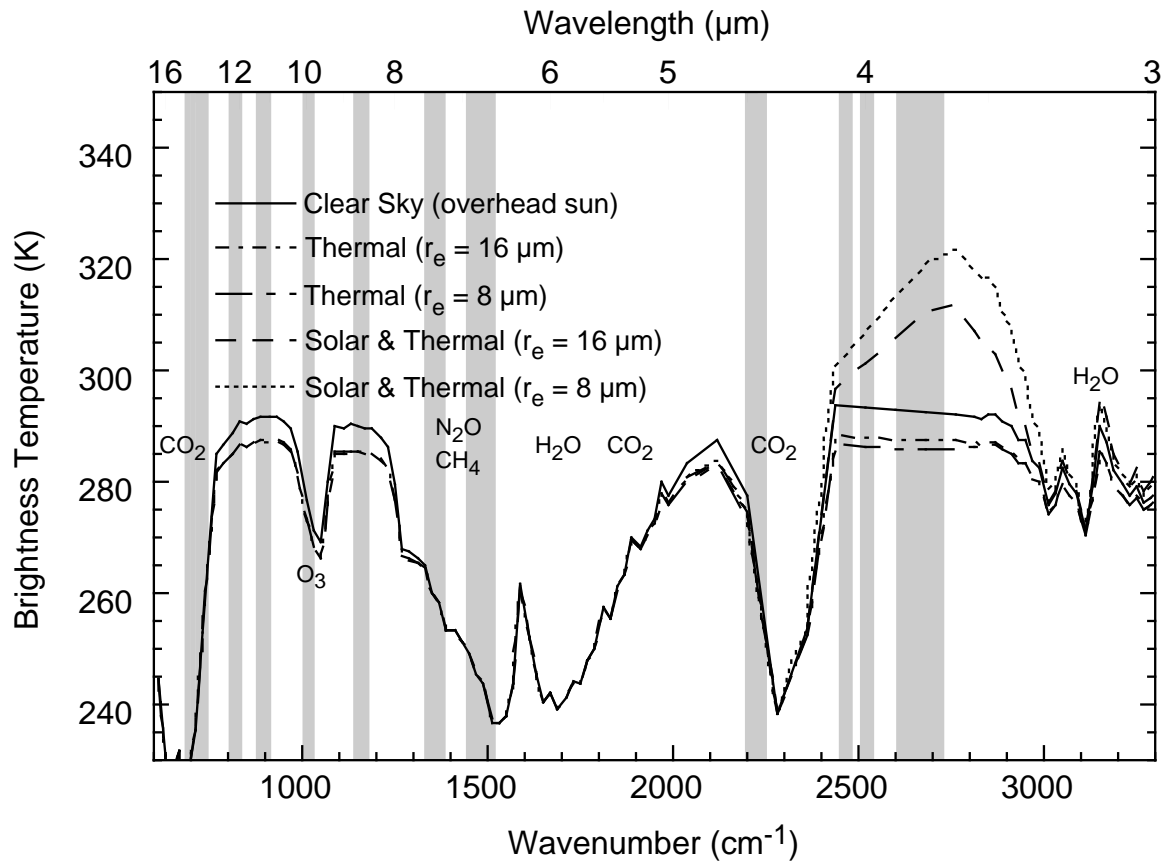


Figure 4. Brightness temperature as a function of wavelength for nadir observations and for various values of the effective radius of cloud droplets, where the cloud optical thickness $\tau_c(0.75 \mu\text{m}) = 5$ for all cases. Results apply to water clouds having a modified gamma distribution embedded in a midlatitude summer atmosphere with cloud top temperature $T_t = 14^\circ\text{C}$, cloud base temperature $T_b = 17^\circ\text{C}$, and an underlying surface temperature $T_s = 21^\circ\text{C}$ (assumed black). The location and bandwidth of all MODIS thermal bands are also shown in the figure.

oxide, ozone, and the infrared water vapor continuum) at a 20 cm^{-1} spectral resolution (Tsay et al. 1989), with a low-level water cloud of optical thickness 5 (at $0.75 \mu\text{m}$) placed at an altitude between 1 and 1.5 km.

In the $3.7 \mu\text{m}$ window, both solar reflected and thermal emitted radiation are significant, though the use of the reflectance for cloud droplet size retrieval is seen to be much more sensitive than the thermal component (note that, in either case, the thermal and solar signals must be separated to provide the desired component). CO_2 absorption is important around $4.3 \mu\text{m}$ and at wavelengths

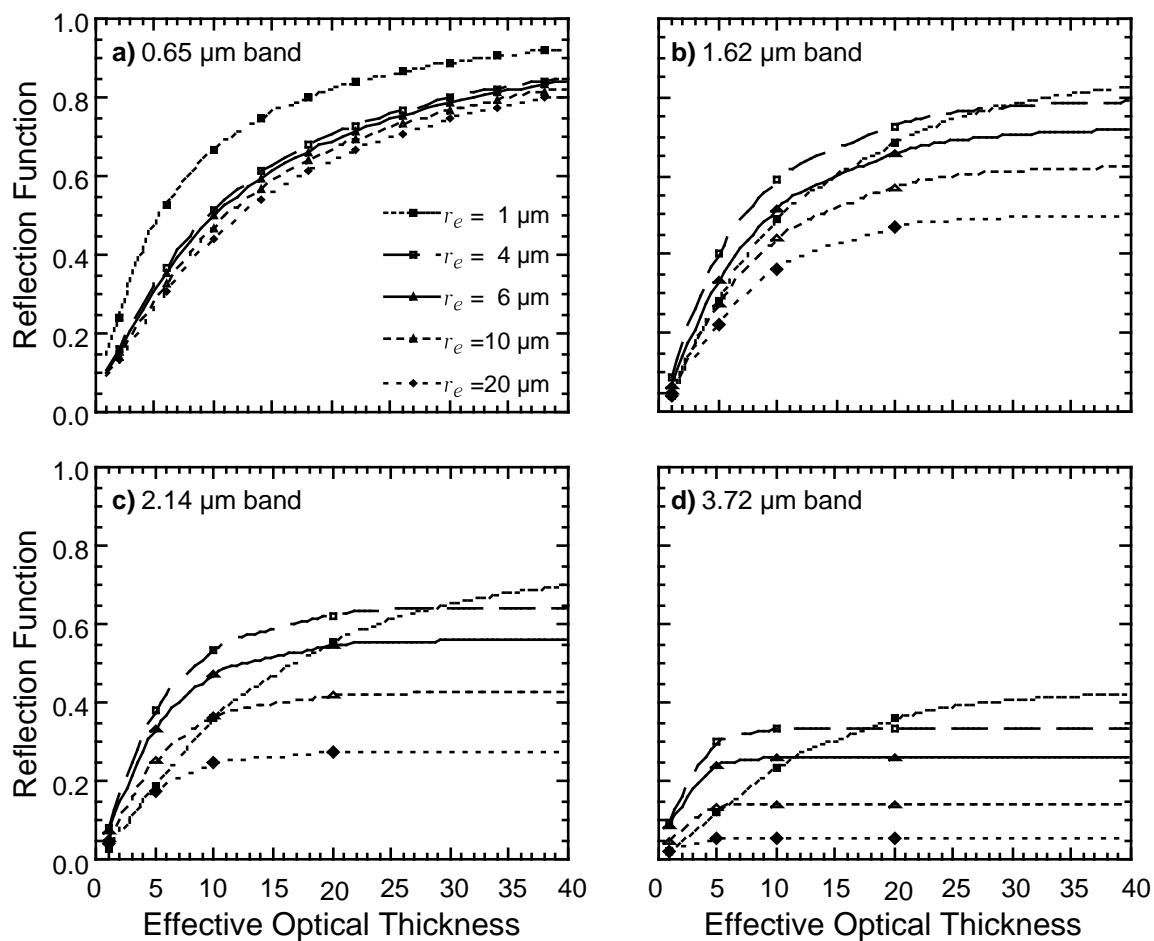


Figure 5. Reflection function as a function of effective optical thickness at a visible wavelength for (a) 0.65 μm , (b) 1.62 μm , (c) 2.14 μm , and (d) 3.72 μm .

greater than about 13 μm ; the MODIS bands in these spectral regions can indicate vertical changes of temperature.

Figure 5 shows the reflection function as a function of optical thickness and effective radius for the MODIS Airborne Simulator bands used in cloud retrieval validation studies. Calculations were performed using the optical constants of liquid water compiled by Irvine and Pollack (1968), together with the assumption that the underlying surface reflectance $A_g = 0.0$. As previously noted, the optical thickness of a cloud depends on wavelength as well as the cloud particle size distribution $n(r)$, as reflected in the effective radius [see King et al. (1990) for an illustration of the spectral dependence of τ_c , g , s and τ_c']. In order to compare the

curves of Fig. 5 for various wavelengths, the optical thickness $\tau_c(\lambda)$ is scaled by $2/Q_{\text{ext}}(r_e/\lambda)$ to provide a common abscissa [roughly equivalent to $\tau_c(\lambda_{\text{vis}})$], where $Q_{\text{ext}}(r_e/\lambda)$ is the extinction efficiency factor. For the visible band, scattering is nearly conservative so that separation of the reflection function curves in Fig. 5a is due to an increasing asymmetry factor with droplet size (for $r_e \gtrsim 4 \mu\text{m}$). For the near-infrared bands, the similarity parameter (and hence droplet absorption) increases approximately linearly with effective radius, and hence the asymptotic reflectance of a cloud decreases with particle size. These figures show that the visible band contains information primarily regarding cloud optical thickness, whereas the absorbing channels eventually reach an optical thickness where they are primarily dependent on particle size alone. A combination of visible and near-infrared absorbing bands therefore provides information on both optical thickness and effective radius.

A close examination of Figs. 5b-d also reveals that the reflection function for a single absorbing wavelength is, in general, not unique. In all near-infrared channels, an effective radius of $1 \mu\text{m}$ is seen to have the same reflection function, at some optical thickness, as some other radius. This has been observed by a number of investigators, all of whom eliminated the small droplet size on the basis of physical arguments that these small sizes do not typically occur in real terrestrial clouds (e.g., Twomey and Cocks 1989, using 1.2, 1.6 and $2.2 \mu\text{m}$; Nakajima and King 1990, using $2.2 \mu\text{m}$; Platnick and Twomey 1994, using $3.7 \mu\text{m}$). Nakajima and King (1990) showed that a combination of 1.6, 2.2 and $3.7 \mu\text{m}$ bands in a single cloud retrieval should eliminate this ambiguity (multivalued solution) in the retrieved particle radius (see below).

b. Cloud thermodynamic phase

During the post-launch time period, we plan to perfect a robust and routine algorithm for determining cloud thermodynamic phase (water *vs* ice). The physical principle upon which this technique is based is the fact that the differences in reflected solar radiation between the 0.645 and 1.64 μm channels contain information regarding cloud particle phase due to distinct differences in bulk absorption characteristics between water and ice at the longer wavelength. The visible reflectance, suffering no appreciable absorption for either ice or liquid water, is relatively unaffected by thermodynamic phase. However, if the cloud is composed of ice, or if the surface is snow covered (similar in effect to large ice particles), then the reflectance of the cloud at 1.64 μm will be smaller than for an otherwise identical liquid water cloud. The 2.13 μm channel is expected to show a significant decrease in reflectance as well, but this is somewhat less dramatic than the reduced reflectance at 1.64 μm . Demonstrations of the application of this method to the problem of distinguishing the thermodynamic phase of clouds can be found in Hansen and Pollack (1970), Curran and Wu (1982), and Pilewskie and Twomey (1987). For added phase discrimination, it is expected that a retrieval of cloud effective radius using the 1.64 μm channel alone will yield a substantially different result than one obtained using only the 2.13 μm channel.

As an example of the sensitivity of the 1.64 and 2.13 μm channels of MODIS to the thermodynamic phase of clouds, we have examined MAS data obtained over the northern foothills of the Brooks Range, Alaska, on 8 June 1996. These data were acquired as part of a NASA ER-2 airborne campaign to study arctic stratus clouds over sea ice in the Beaufort Sea. The panel in the upper left portion of Fig. 6, acquired at 0.66 μm , shows high contrast between an optically thick convective cumulonimbus cloud in the center of the image, a diffuse cirrus anvil

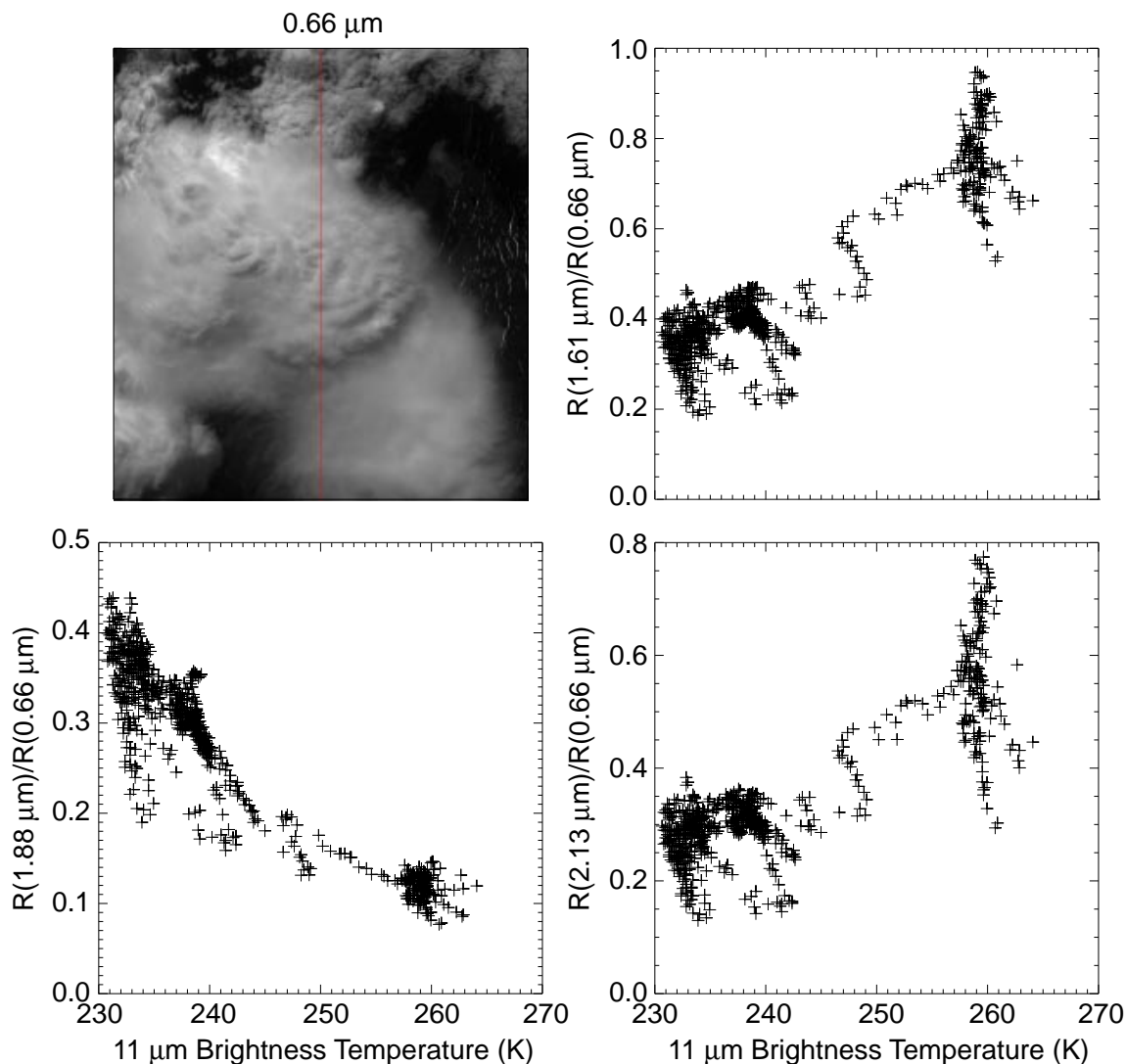


Figure 6. The upper left-hand panel shows a MAS 0.66 μm image of a convective cumulonimbus cloud surrounded by lower-level water clouds on the north slope of the Brooks Range on 7 June 1996. Subsequent panels show scatter plots of the reflection function ratio $R^{1.61}/R^{0.66}$, $R^{1.88}/R^{0.66}$, and $R^{2.13}/R^{0.66}$ as a function of the corresponding brightness temperature at 11.02 μm for nadir observations of the MAS over a cloud scene containing both water and ice clouds.

in the lower part of the image, less reflective altocumulus clouds in the upper part of the image, and dark tundra. From data obtained down the nadir track of the aircraft (vertical line down the center of the image), we have produced scatter plots of the ratio of the reflection function at 1.61, 1.88, and 2.13 μm to that at 0.66 μm as a function of the brightness temperature at 11.02 μm . These observations

clearly shows that the cold portion of the scene contained ice particles (low reflectance at 1.61 and 2.13 μm), whereas the warm portion contained water droplets (high reflectance at 1.61 and 2.13 μm), as expected. In addition, the 1.88 μm channel, the closest analog to the 1.38 μm water vapor absorbing channel on MODIS, suggests that the colder ice clouds were high in the atmosphere (high 1.88 μm reflectance), whereas the warmer water clouds were low in the atmosphere (low 1.88 μm reflectance).

c. Ice cloud properties

After the cloud mask and phase determination, the physical and optical properties of ice clouds can, in principle, be retrieved in a manner similar to that described previously for water clouds. Under the assumption of plane-parallel geometry, two other factors complicate the retrievals of ice cloud properties (viz., the shape and orientation of the ice particles) occurring naturally in the atmosphere. Due to our limited knowledge accumulated thus far for ice clouds, the sensitivity of their retrieved properties on these two factors is still an ongoing research subject.

Following the same manner as in water clouds, we have selected a size distribution of the ice particles for the purpose of discussion. Figure 7 shows an observed size distribution for averaged cirrus clouds obtained during the FIRE-II Cirrus IFO on 5 December 1991. This model cloud is composed of 50% bullet rosettes, 30% hollow columns, and 20% solid plate ice crystals. We then define the effective particle diameter as follows

$$D_e = \int_0^{\infty} LD^2n(L)dL / \int_0^{\infty} LDn(L)dL, \quad (6)$$

where D and L denote the width and the maximum dimension of an ice crystal,

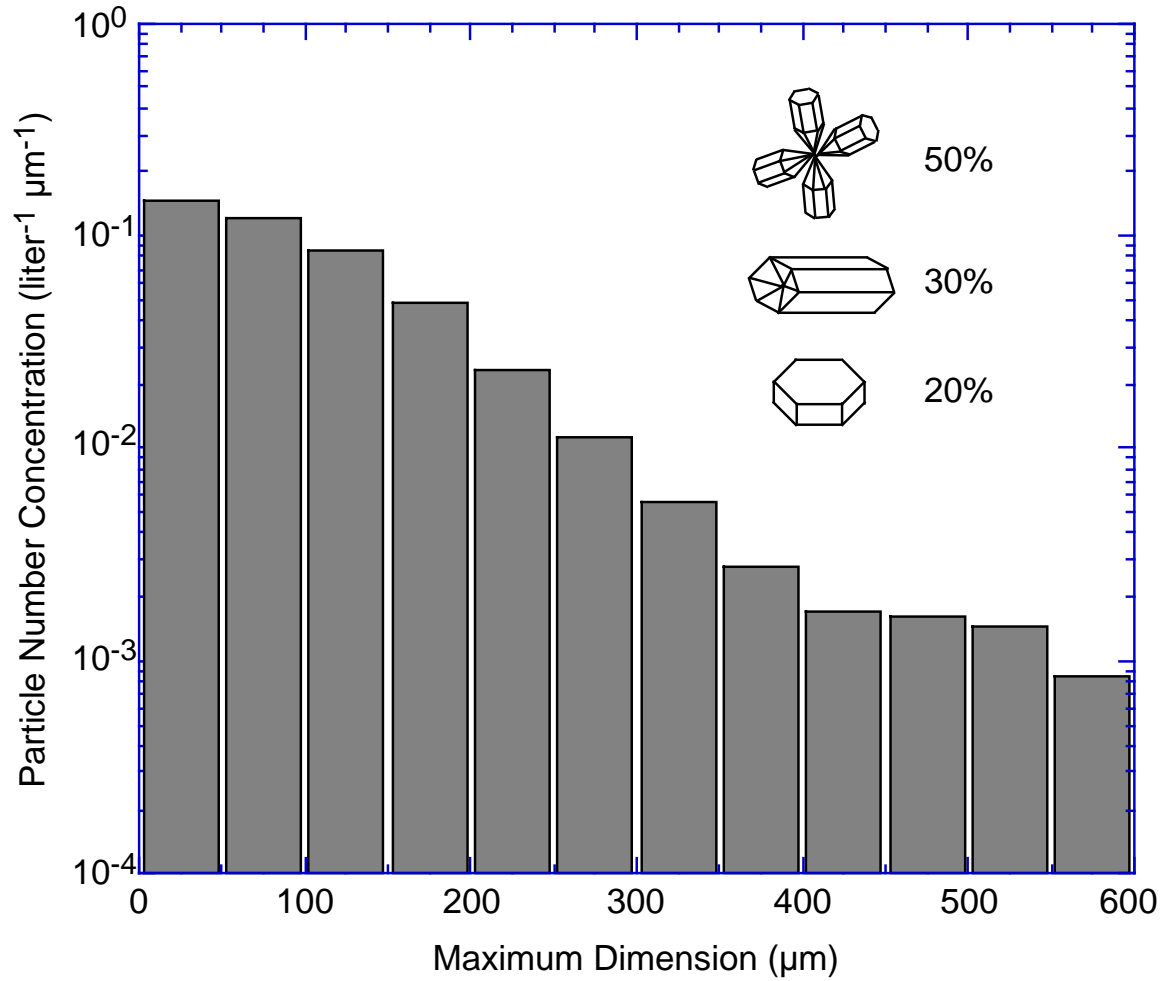


Figure 7. An averaged ice-crystal size distribution observed during the FIRE-II Cirrus IFO (5 December 1991), as determined from the replicator sounding.

respectively, and $n(L)$ is the size distribution as a function of L . The rationale for defining D_e to represent ice-crystal size distribution is that the scattering of light is related to the geometric cross section, which is proportional to LD . To calculate properties of light scattering and absorption by ice crystals, we have adopted a unified theory developed by Takano and Liou (1989, 1995), and Yang and Liou (1995, 1996a,b) for all sizes and shapes. This unified theory is a unification of an improved geometric ray-tracing/Monte Carlo method for size parameters larger than about 15 and a finite-difference time domain method for size parameters less than 15.

Table 2. Optical properties of a representative ice crystal size distribution for six MODIS channels.

Channel	λ (μm)	m_r	m_i	β_e	ω_0	g
1	0.645	1.3082	1.325×10^{-8}	0.32827	0.99999	0.84580
5	1.240	1.2972	1.22×10^{-5}	0.33141	0.99574	0.85224
6	1.640	1.2881	2.67×10^{-4}	0.32462	0.93823	0.87424
7	2.130	1.2674	5.65×10^{-4}	0.32934	0.91056	0.89044
20	3.750	1.3913	6.745×10^{-3}	0.32971	0.68713	0.90030
31	11.030	1.1963	2.567×10^{-1}	0.32812	0.54167	0.95739

In Table 2, we demonstrate the bulk optical properties of this ice cloud model, calculated for six selected MODIS channels. Their corresponding phase functions are illustrated in Fig. 8. Thus, the reflected reflectance fields [e.g., Eq. (5)] for ice clouds can be pre-computed for later use in retrieval algorithms similar to those of water clouds. It is worth noting that Ou et al. (1993) recently developed a retrieval technique that utilizes the thermal infrared emission of ice clouds to determine their optical thickness and effective particle size. Removal of the solar component in the 3.75 μm intensity is required for daytime applications, which is made by correlating the 3.75 μm (solar) and 0.645 μm reflectances. However, it is clear that the use of the reflectance for particle size retrieval is seen from Fig. 4 to be much more sensitive than the thermal infrared component. Careful intercomparison of cloud retrievals between these two methods is currently underway.

3.1.2. Mathematical description of algorithm

a. Asymptotic theory for thick layers

In the case of optically thick layers overlying a Lambertian surface, the expression for the reflection function of a conservative scattering atmosphere can be written as (King 1987)

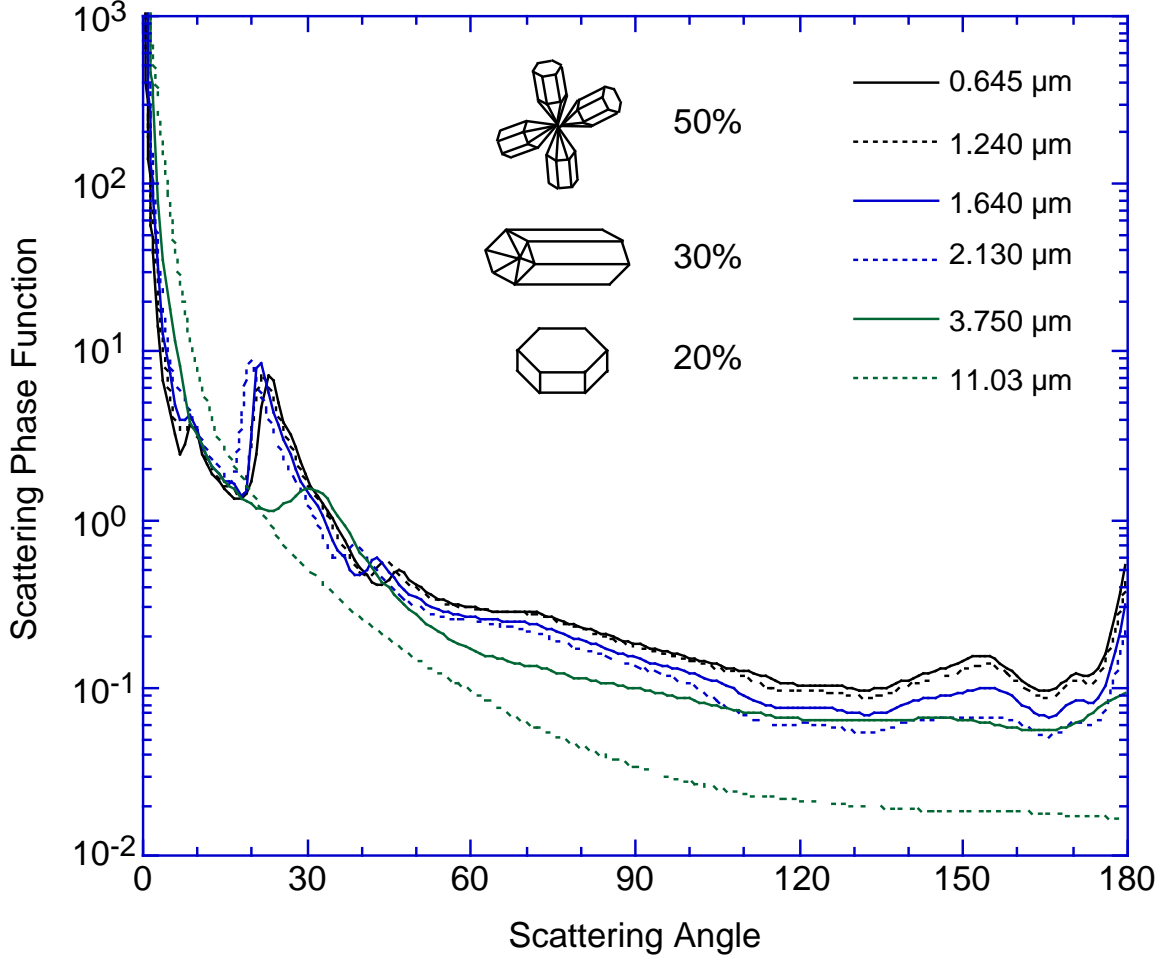


Figure 8. Scattering phase functions for the ice cloud model shown in Fig. 7, calculated for six selected MODIS channels.

$$R(\tau_c; \mu, \mu_0, \phi) = R_\infty(\mu, \mu_0, \phi) - \frac{4(1-A_g)K(\mu)K(\mu_0)}{[3(1-A_g)(1-g)(\tau_c+2q_0) + 4A_g]}, \quad (7)$$

from which the scaled optical thickness τ_c' can readily be derived:

$$\tau_c' = (1-g)\tau_c = \frac{4K(\mu)K(\mu_0)}{3[R_\infty(\mu, \mu_0, \phi) - R(\tau_c; \mu, \mu_0, \phi)]} - 2q' - \frac{4A_g}{3(1-A_g)}. \quad (8)$$

In these expressions $R(\tau_c; \mu, \mu_0, \phi)$ is the measured reflection function at a nonabsorbing wavelength, $R_\infty(\mu, \mu_0, \phi)$ the reflection function of a semi-infinite atmosphere, $K(\mu)$ the escape function, A_g the surface (ground) albedo, g the asymmetry factor, and q_0 the extrapolation length for conservative scattering. The reduced extrapolation length $q' = (1-g)q_0$ lies in the range 0.709 to 0.715 for

all possible phase functions (van de Hulst 1980), and can thus be regarded as a constant ($q' \approx 0.714$).

From Eq. (8) we see that the scaled optical thickness of a cloud depends on q' , A_g , $K(\mu)$ and the *difference* between $R_\infty(\mu, \mu_0, \phi)$ and the measured reflection function. At water-absorbing wavelengths outside the molecular absorption bands (such as 1.64, 2.13 and 3.75 μm), the reflection function of optically thick atmospheres overlying a Lambertian surface can be expressed as (King 1987)

$$R(\tau_c; \mu, \mu_0, \phi) = R_\infty(\mu, \mu_0, \phi) - \frac{m[(1-A_g A^*)l - A_g m n^2]K(\mu)K(\mu_0)e^{-2k\tau_c}}{[(1-A_g A^*)(1-l^2 e^{-2k\tau_c}) + A_g m n^2 l e^{-2k\tau_c}]}, \quad (9)$$

where k is the diffusion exponent (eigenvalue) describing the attenuation of radiation in the diffusion domain, A^* the spherical albedo of a semi-infinite atmosphere, and m, n and l constants. All five asymptotic constants that appear in this expression [A^*, m, n, l and $k/(1-g)$] are strongly dependent on the single scattering albedo ω_0 , with a somewhat weaker dependence on g . In fact, van de Hulst (1974, 1980) and King (1981) showed that these constants can be well represented by a function of a similarity parameter s , defined by Eq. (3), where s reduces to $(1 - \omega_0)^{1/2}$ for isotropic scattering and spans the range 0 ($\omega_0 = 1$) to 1 ($\omega_0 = 0$). Similarity relations for the asymptotic constants that arise in Eqs. (7-9) can be found in King et al. (1990), and can directly be computed using eigenvectors and eigenvalues arising in the discrete ordinates method (Nakajima and King 1992).

b. Retrieval example

To assess the sensitivity of the reflection function to cloud optical thickness and effective radius, we performed radiative transfer calculations for a wide variety of solar zenith angles and observational zenith and azimuth angles at selected wavelengths in the visible and near-infrared. Figure 9a (9b) shows repre-

sentative calculations relating the reflection functions at 0.664 and 1.621 μm (2.142 μm). These wavelengths were chosen because they are outside the water vapor and oxygen absorption bands and yet have substantially different water droplet (or ice particle) absorption characteristics (cf. Fig. 2). These wavelengths

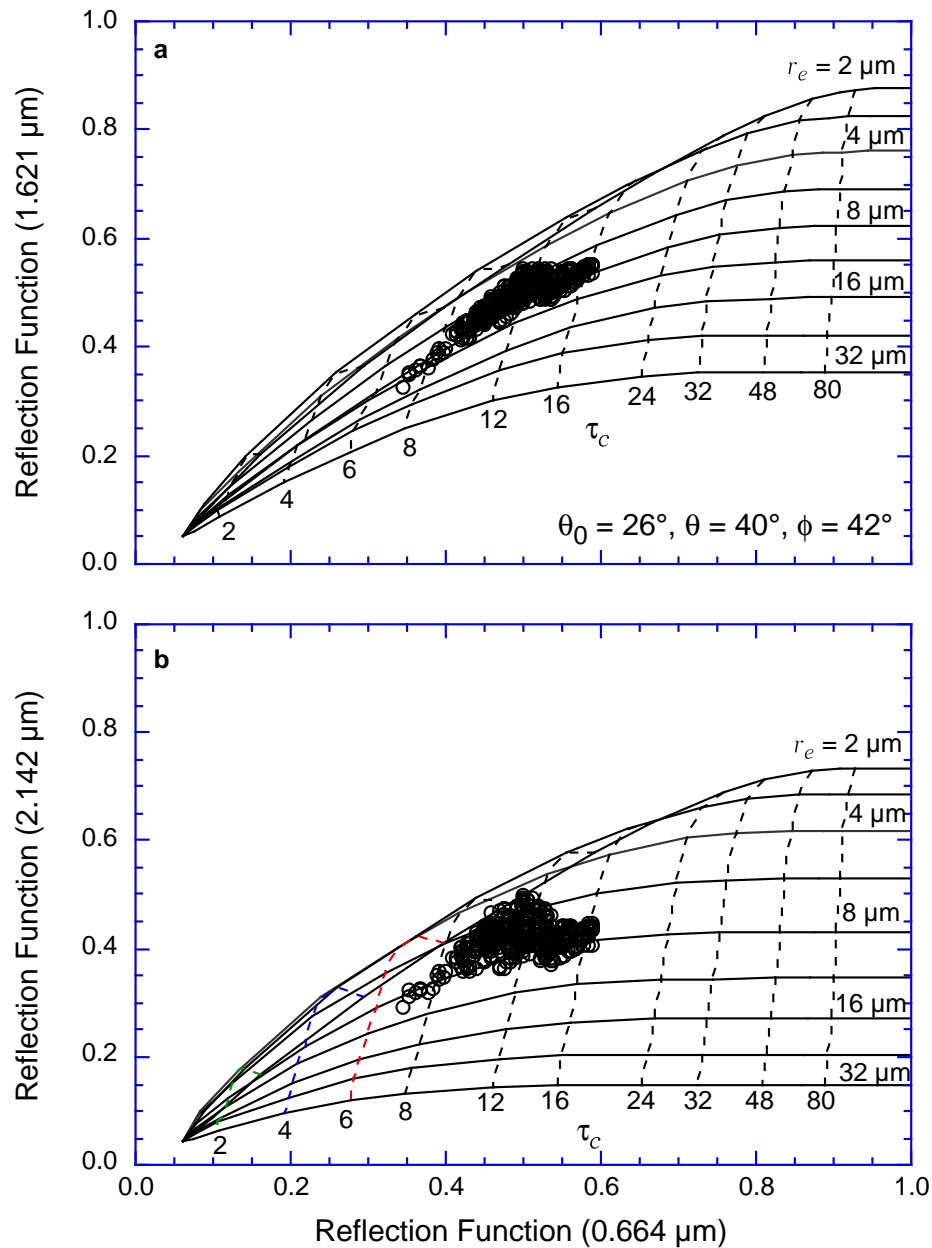


Figure 9. Theoretical relationship between the reflection function at 0.664 and (a) 1.621 μm and (b) 2.142 μm for various values of τ_c (at 0.664 μm) and r_e when $\theta_0 = 26^\circ$, $\theta = 40^\circ$ and $\phi = 42^\circ$. Data from measurements above marine stratocumulus clouds during ASTEX are superimposed on the figure (22 June 1992).

correspond to three channels of the MAS, but may readily be adapted to the comparable 0.645, 1.64, 2.13 and 3.75 μm channels of MODIS.

Figure 9 clearly illustrates the underlying principles behind the simultaneous determination of τ_c and r_e from reflected solar radiation measurements. The minimum value of the reflection function at each wavelength corresponds to the reflection function of the underlying surface at that wavelength in the absence of an atmosphere. For the computations presented in Fig. 9, the underlying surface was assumed to be Lambertian with $A_g = 0.06, 0.05$, and 0.045 for wavelengths of $0.664, 1.621$, and $2.142 \mu\text{m}$, respectively, roughly corresponding to an ocean surface. The dashed curves in Fig. 9 represent the reflection functions at $0.664, 1.621$ and $2.142 \mu\text{m}$ that result for specified values of the cloud optical thickness at $0.664 \mu\text{m}$. The solid curves, on the other hand, represent the reflection functions that result for specified values of the effective particle radius. These results show, for example, that the cloud optical thickness is largely determined by the reflection function at a nonabsorbing wavelength ($0.664 \mu\text{m}$ in this case), with little dependence on particle radius. The reflection function at $2.142 \mu\text{m}$ (or $1.621 \mu\text{m}$), in contrast, is largely sensitive to r_e , with the largest values of the reflection function occurring for small particle sizes. In fact, as the optical thickness increases ($\tau_c \gtrsim 12$), the sensitivity of the nonabsorbing and absorbing channels to $\tau_c(0.664 \mu\text{m})$ and r_e is very nearly orthogonal. This implies that under these optically thick conditions we can determine the optical thickness and effective radius nearly independently, and thus measurement errors in one channel have little impact on the cloud optical property determined primarily by the other channel. The previously described multiple solutions are clearly seen as r_e and τ_c decrease.

The data points superimposed on the theoretical curves of Fig. 9 represent

over 400 measurements obtained with the MAS, a 50-channel scanning spectrometer that was mounted in the right wing superpod of the NASA ER-2 aircraft during ASTEX. These observations were obtained as the aircraft flew over marine stratocumulus clouds in the vicinity of the Azores approximately 1000 km southwest of Lisbon on 22 June 1992.

c. Atmospheric corrections: Rayleigh scattering

As discussed in the previous section, the sensor-measured intensity at visible wavelengths ($0.66\ \mu\text{m}$) is primarily a function of cloud optical thickness, whereas near-infrared intensities (1.6 , 2.1 , and $3.7\ \mu\text{m}$) are sensitive both to optical thickness and, especially, cloud particle size. As a consequence, Rayleigh scattering in the atmosphere above the cloud primarily affects the cloud optical thickness retrieval since the Rayleigh optical thickness in the near-infrared is negligible. Because the Rayleigh optical thickness in the visible wavelength region is small (about 0.044 at $0.66\ \mu\text{m}$), it is frequently overlooked in retrieving cloud optical thickness.

We simplified the air-cloud system as a two-layer atmosphere with molecules above the cloud, and carried out simulations with an adding-doubling code to investigate the Rayleigh scattering effects on cloud optical thickness retrievals. Figures 10a and 10b provide typical errors $\Delta\tau_c$ (%) in retrieved cloud optical thickness τ_c without making any Rayleigh corrections. These errors apply to a cloud with an effective particle radius $r_e = 8\ \mu\text{m}$. Figure 10a applies to errors $\Delta\tau_c$ (%) at different solar and viewing zenith angles when $\tau_c = 2$, whereas Figure 10b pertains to $\Delta\tau_c$ (%) for different solar angles and various cloud optical thicknesses when the viewing zenith angle $\theta = 45.2^\circ$. Figure 10a shows that, for a thin cloud layer, $\Delta\tau_c$ ranges between 15 and 60% for solar and viewing angles ranging

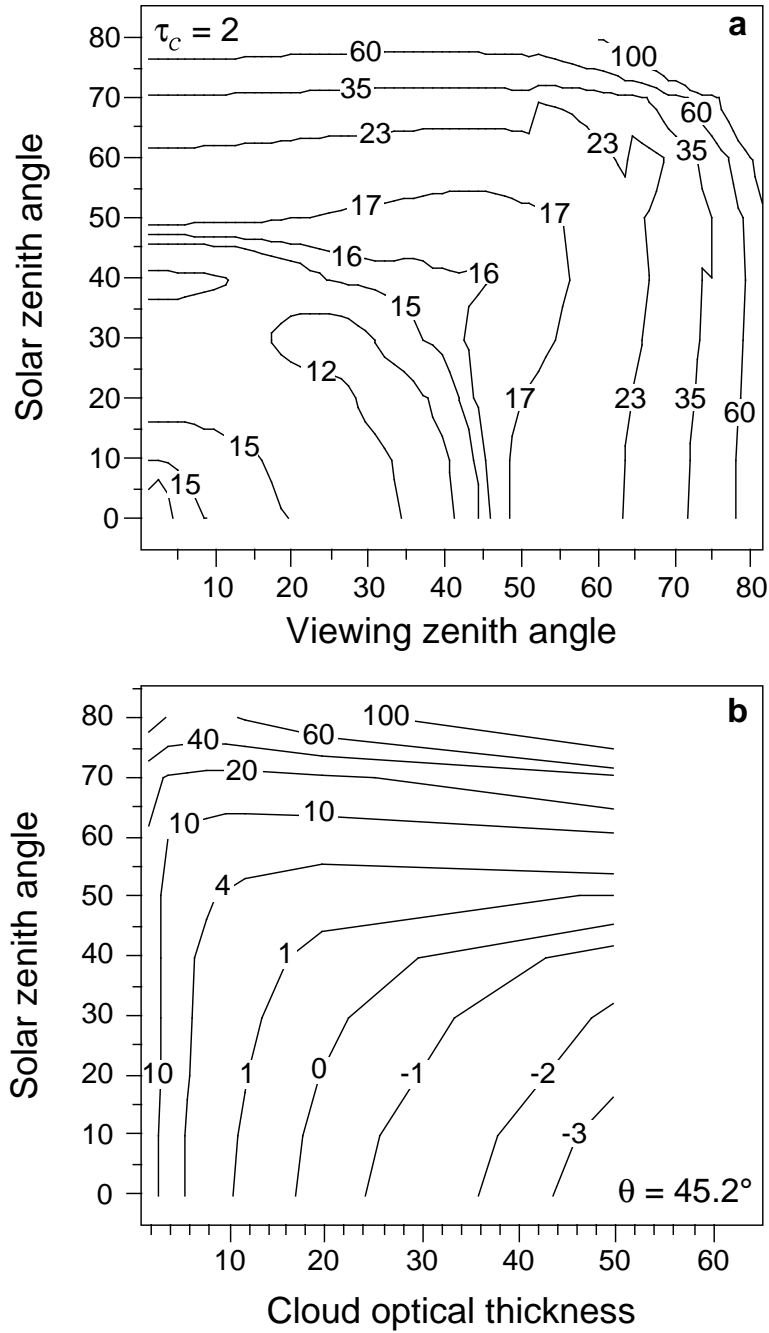


Figure 10. Error $\Delta\tau_c$ (%) in retrieved cloud optical thickness without Rayleigh corrections for (a) $\tau_c = 2$ and (b) $\theta = 45.2^\circ$. The azimuth angle $\phi = 90^\circ$ in both cases.

from 0-80°. Errors increase with increasing solar and/or viewing angles because of enhanced Rayleigh scattering contributions at large angles. On the other hand, Figure 10b shows that, for thick clouds, $\Delta\tau_c$ still can be as high as 10-60% shows that, for thick clouds, $\Delta\tau_c$ still can be as high as 10-60% for solar zenith an-

gles $\theta_0 \geq 60^\circ$. Therefore, it is important to correct for Rayleigh scattering contributions to the reflected signal from a cloud layer both for (i) the case of thin clouds, and (ii) for large solar zenith angles and all clouds.

We developed an iterative method for effectively removing Rayleigh scattering contributions from the measured intensity signal in cloud optical thickness retrievals (Wang and King 1996). In brief, by assuming that no multiple scattering occurs in the Rayleigh layer, we decomposed the sensor-measured upward reflection function of the two-layer air-cloud atmosphere at the top of the atmosphere arising from (i) direct Rayleigh single scattering without reflection from the cloud, (ii) contributions of single interactions between air molecules and clouds, and (iii) reflection of the direct solar beam from the cloud. By removing contributions (i) and (ii) from the sensor-measured reflection function, we were able to derive iteratively the cloud top reflection function in the absence of Rayleigh scattering for use in cloud optical thickness retrievals. The Rayleigh correction algorithm has been extensively tested for realistic cloud optical and microphysical properties with different solar zenith angles and viewing geometries. From simulated results we concluded that, with the proposed Rayleigh correction algorithm, the error in retrieved cloud optical thickness was reduced by a factor of 2 to over 10 for both thin clouds as well as thick clouds with large solar zenith angles. The iteration scheme is efficient and has been incorporated into our cloud retrieval algorithm.

d. Atmospheric corrections: Water vapor

The correlated k -distribution of Kratz (1995) can be used to calculate the gaseous atmospheric transmission and/or emission for all MODIS channels. The primary input for this code is an atmospheric temperature and water vapor pro-

file for the above-cloud portion of the atmosphere. It is expected that temperature and humidity can be provided by other MODIS products (MOD07 for the nearest clear sky pixel) or perhaps ancillary sources. Alternatively, it may turn out that many of the MODIS channels are not particularly sensitive to the distribution of water vapor, but only to the column amount. For such channels, above-cloud precipitable water estimates from MOD05 may be sufficient. Estimates of ozone amount, from either MOD07 or ancillary sources, will be needed for the 0.645 μm channel if standard values prove insufficient.

The effects of the atmosphere need to be removed so that the cloud-top reflectance and/or emission can be determined. It is these cloud-top quantities that are stored in the libraries of Fig. 11 (see below). Ignoring Rayleigh or aerosol scattering, gaseous absorption in the above-cloud atmosphere can be accounted for with the following equation (Platnick and Valero 1995):

$$\begin{aligned}
 I(\mu, \mu_0, \phi) = & I_{\text{cloud-top}}^{\text{solar}}(\tau_c, r_e, A_g; \mu, \mu_0, \phi) t_{\text{atm}}(\mu) t_{\text{atm}}(\mu_0) \\
 & + I_{\text{atm}}^{\text{solar}}(\mu, \mu_0, \phi) + I_{\text{cloud-top}}^{\text{emission}}(\tau_c, r_e, A_g; \mu) t_{\text{atm}}(\mu) \\
 & + I_{\text{atm}}^{\text{emission}}(\mu),
 \end{aligned} \tag{10}$$

where I is the measured intensity at the top-of-atmosphere, $I_{\text{cloud-top}}$ is the cloud-top intensity, including surface effects, in the absence of an atmosphere, and t_{atm} is the above-cloud transmittance in either the μ or μ_0 directions. In general, both the cloud and atmosphere contribute emitted (I^{emission}) and solar scattered (I^{solar}) radiant energy. The first term accounts for the effect of the atmosphere on the net cloud-surface reflectance and the third term the effect of cloud and surface emission. For the 3.75 μm channel both scattered solar and emitted thermal terms are needed; for shorter wavelength channels, only solar terms are needed; in the thermal infrared, only emission terms are needed.

Though not strictly correct, it is assumed that in practice this gaseous absorption layer can be treated as separate from the Rayleigh scattering layer described above (or any aerosol layer), such that the specific corrections can be applied independently.

e. Technical outline of multichannel algorithm

A generalized schematic description of the cloud retrieval algorithm is given in Figs. 11-13. Figure 11 shows the steps involved in calculating the reflection

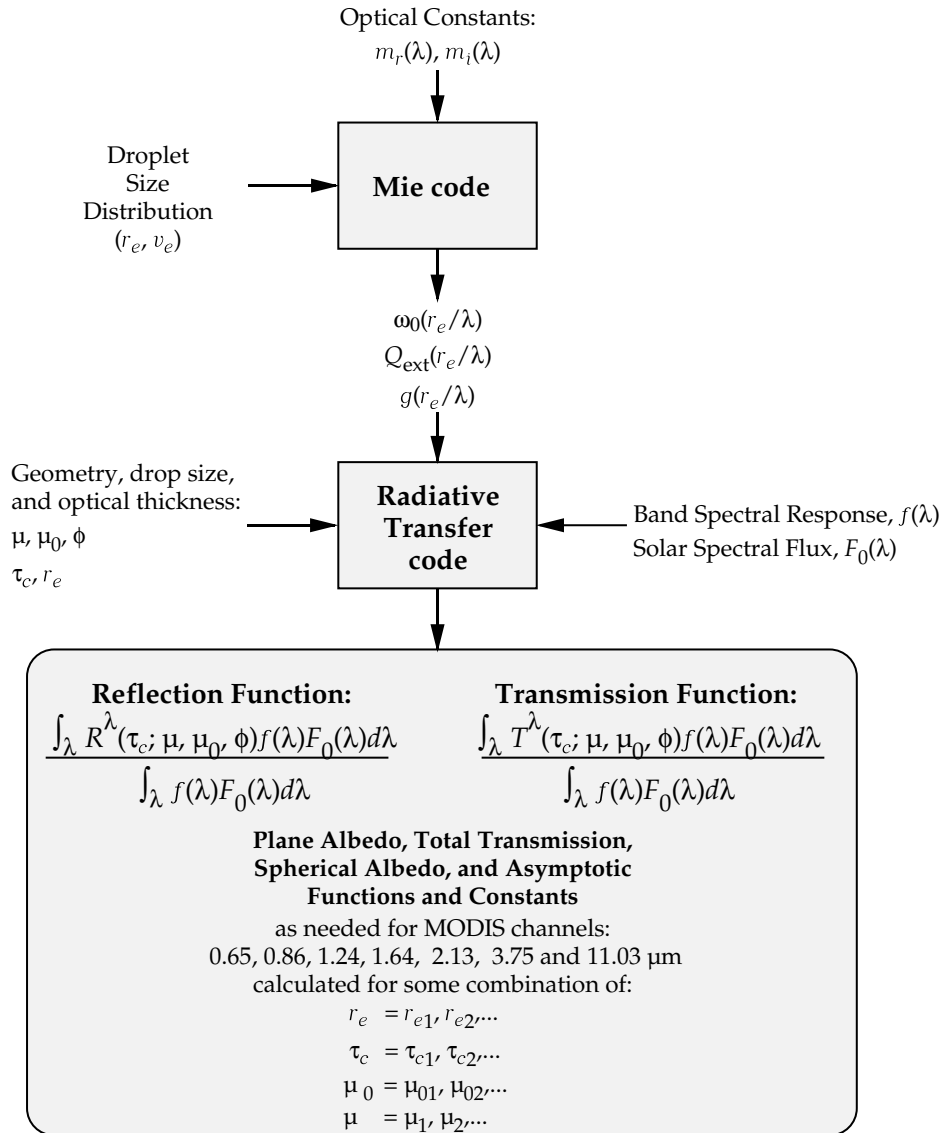


Figure 11. Schematic for generating the reflection function, transmission function, plane albedo, spherical albedo, and asymptotic function parameter library.

function, transmission function, and spherical albedo libraries, including (i) the use of a Mie theory (or nonspherical ice scattering) code for determining optical parameters (ω_0 , Q_{ext} , g and/or phase function) from the optical constants of water, and (ii) a radiative transfer code for determining the reflection function, transmission function, spherical albedo, and asymptotic functions and constants as a function of r_e , τ_c , and geometry.

In computing the optical constants for liquid water, we used complex refractive indices tabulated by Hale and Querry (1973) for wavelengths in the range $0.25 \leq \lambda \leq 0.69 \mu\text{m}$, Palmer and Williams (1974) for $0.69 < \lambda \leq 2.0 \mu\text{m}$, and Downing and Williams (1975) for $\lambda > 2.0 \mu\text{m}$. The natural log-normal size distribution for water droplets was used for all computations with an effective variance $v_e = 0.13$. The influence of surface reflectance is calculated by assuming that the cloud is vertically homogeneous with a surface that reflects radiation according to Lambert's law with ground albedo A_g as

$$R(\tau_c, r_e; \mu, \mu_0, \phi) = R_{\text{cloud}}(\tau_c, r_e; \mu, \mu_0, \phi) + \frac{A_g}{1 - A_g \bar{r}_{\text{cloud}}(\tau_c, r_e)} t_{\text{cloud}}(\tau_c, r_e; \mu) t_{\text{cloud}}(\tau_c, r_e; \mu_0), \quad (11)$$

where $R_{\text{cloud}}(\tau_c, r_e; \mu, \mu_0, \phi)$, $t_{\text{cloud}}(\tau_c, r_e; \mu_0)$, and $\bar{r}_{\text{cloud}}(\tau_c, r_e)$ are, respectively, the reflection function, total transmission (diffuse plus direct), and spherical albedo of a cloud layer when $A_g = 0$. Eq. (11) simplifies the computations of $R(\tau_c, r_e; \mu, \mu_0, \phi)$ for different surface types with lookup libraries of $R_{\text{cloud}}(\tau_c, r_e; \mu, \mu_0, \phi)$, $t_{\text{cloud}}(\tau_c, r_e; \mu_0)$, and $\bar{r}_{\text{cloud}}(\tau_c, r_e)$ for various cloud microphysical and optical properties and for different solar and viewing geometries.

The asymptotic functions and constants that appear in Eqs. (7)-(9) can readily be determined either following radiative transfer computations, using the asymptotic fitting method of van de Hulst (1980), or directly from the Mie code

using the coefficients of the Legendre polynomial expansion of the phase function, as described by Nakajima and King (1992).

Figure 12 shows an algorithm for retrieving r_e and τ_c from comparisons of measured reflection functions with entries in the library. The definition of the residual used for determining the best fit is typically defined as a least-squares

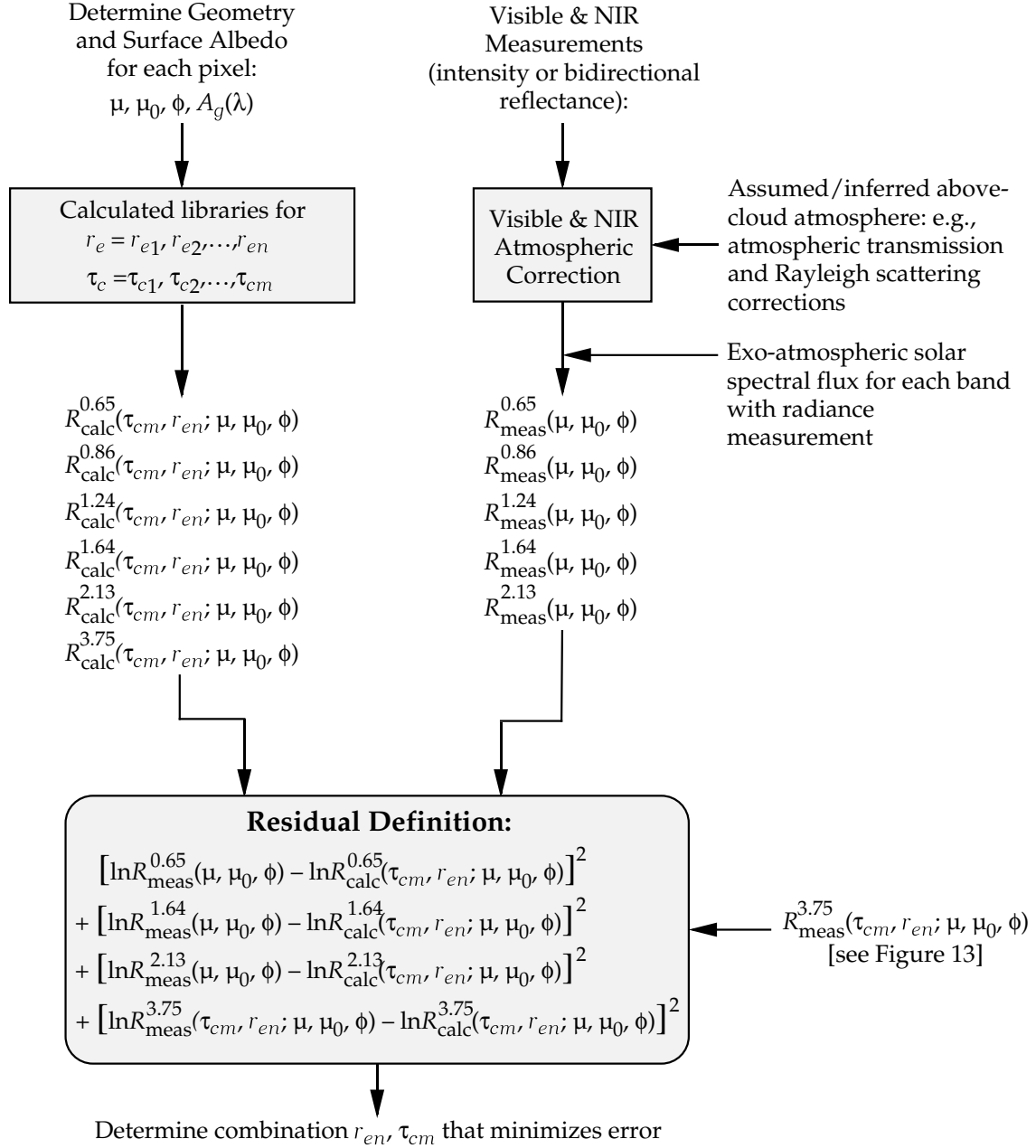


Figure 12. A general cloud retrieval algorithm for determining best fit for r_e and τ_c in the 0.65, 1.64 and 2.13 μm bands.

fit, and is often a weighted fit (Twomey and Cocks 1989).

The use of the 3.75 μm band complicates the algorithm because radiation emitted by the cloud is comparable to, and often dominates, the solar reflectance. Cloud emission at 3.75 μm is weakly dependent on r_e , unlike solar reflectance (cf. Fig. 4), so the relative strength of the two depends on particle size. Surface emission can also be significant for thin clouds ($\tau_c \lesssim 5$). For example, with cloud and surface temperatures of 290 K, emission and reflectance are approximately equal for $r_e = 10 \mu\text{m}$ (Platnick and Twomey 1994). An assumption that is often made is that clouds are isothermal. Retrievals using this channel include those made by Arking and Childs (1985), Grainger (1990), Platnick (1991), Kaufman and Nakajima (1993), Han et al. (1994, 1995), Platnick and Valero (1995), and Nakajima and Nakajima (1995), all of whom used the visible and 3.7 μm channels of AVHRR.

To correct for thermal emission in the 3.75 μm band, we decomposed the total upward reflection function at the top of the atmosphere into solar, thermal, and surface contributions. Ignoring atmospheric effects above the cloud, which can readily be corrected as described above for both water vapor and Rayleigh scattering effects, we can write the total above-cloud measured reflection function as (Platnick and Valero 1995; Nakajima and Nakajima 1995)

$$\begin{aligned}
 R_{\text{meas}}(\tau_c, r_e; \mu, \mu_0, \phi) = & R_{\text{cloud}}(\tau_c, r_e; \mu, \mu_0, \phi) \\
 & + \frac{A_g}{1 - A_g \bar{r}_{\text{cloud}}(\tau_c, r_e)} t_{\text{cloud}}(\tau_c, r_e; \mu) t_{\text{cloud}}(\tau_c, r_e; \mu_0) \\
 & + \varepsilon_{\text{cloud}}^*(\tau_c, r_e; \mu) B(T_c) \frac{\pi}{\mu_0 F_0} + \varepsilon_{\text{surface}}^*(\tau_c, r_e; \mu) B(T_g) \frac{\pi}{\mu_0 F_0}. \quad (12)
 \end{aligned}$$

In this equation, the first two terms account for solar reflectance and are identical to Eq. (11), $\varepsilon_{\text{surface}}^*(\tau_c, r_e; \mu)$ is the effective surface emissivity that includes the effect of the cloud on radiation emitted by the surface, and $\varepsilon_{\text{cloud}}^*(\tau_c,$

$r_e; \mu$) is the effective cloud emissivity that can be formulated to include cloud emission that is reflected by the surface. These emissivities are given by

$$\begin{aligned} \varepsilon_{\text{cloud}}^*(\tau_c, r_e; \mu) = & [1 - t_{\text{cloud}}(\tau_c, r_e; \mu) - r_{\text{cloud}}(\tau_c, r_e; \mu)] \\ & + \text{surface interaction terms}, \end{aligned} \quad (13)$$

$$\varepsilon_{\text{surface}}^*(\tau_c, r_e; \mu) = \frac{1 - A_g}{1 - A_g \bar{r}_{\text{cloud}}(\tau_c)} t_{\text{cloud}}(\tau_c, r_e; \mu), \quad (14)$$

where $r_{\text{cloud}}(\tau_c, r_e; \mu)$ is the plane albedo of the cloud, and $B(T_c)$ and $B(T_g)$ are, respectively, the Planck function at cloud top temperature T_c and surface temperature T_g .

The terms on the right-hand side of Eq. (12) pertain, in turn, to (i) solar reflection by the cloud in the absence of surface reflection, (ii) contributions from multiple reflection of solar radiation by the Earth's surface, (iii) thermal emission from the cloud, and (iv) thermal emission from the surface. For thin clouds ($\tau_c \lesssim 5$), the first and fourth terms dominate, with surface emission contributing over 50% of the total measured intensity. For thick clouds ($\tau_c > 10$), on the other hand, the first and third terms are the most important. The surface interaction terms in the effective cloud emissivity account for downward emitted cloud radiation reflected by the surface and back through the cloud. This is generally insignificant except for perhaps the optically thinnest clouds. The cloud top temperature T_c can be obtained either by converting the intensity measured at $11.03 \mu\text{m}$ or as an output of Menzel and Strabala's (ATBD-MOD-04) MODIS cloud top property product. Surface temperature T_g is also required under cloudy conditions, and we intend to obtain this parameter from $11.03 \mu\text{m}$ intensity measurements at nearby cloud free pixels. This is only a serious problem for optically thin (i.e., cirrus) clouds.

The thermal emission from the atmosphere above the cloud [the third term

in Eq. (10)] is usually of second order importance, contributing only a few percent to the total intensity. This emission can be expressed as

$$R_{\text{atm}}(\mu) = -\frac{\pi}{\mu_0 F_0} \int_0^{p_0} B(T(p)) \, dt_{\text{atm}}(p; \mu), \quad (15)$$

$$\approx \frac{\pi}{\mu_0 F_0} [1 - t_{\text{atm}}(\mu)] B(T_a), \quad (16)$$

where p_0 is the cloud top pressure and T_a is an appropriate atmospheric temperature. For a given temperature and moisture profiles, either obtained from Menzel and Gumley's (ATBD-MOD-07) MODIS atmospheric profiles product (cf. Fig. 1), or from an NCEP gridded data set, we can calculate the $R_{\text{atm}}(\mu)$ term using Eq. (15). An alternative approach is to use Eq. (16) with a given total water-vapor loading above the cloud and some averaged atmospheric temperature. This probably will be accurate enough because of relatively small thermal contributions from atmosphere. By removing the thermal contributions (the third and fourth terms) from the sensor-measured intensity, the 3.75 μm algorithm operates in a manner quite similar to that for the 1.64 and 2.13 μm bands.

We plan on utilizing Nakajima and King's (1990) algorithm for retrieving the cloud optical thickness and effective radius using the 1.64 and 2.13 μm bands, together with a similar algorithm based on Platnick (1991) and Nakajima and Nakajima (1995) for removing the thermal contributions from the 3.75 μm band, as outlined above and in Figure 13.

f. Retrieval of cloud optical thickness and effective radius

In the description of the algorithm that follows, all subsequent references to τ_c will be scaled, or normalized, to an optical thickness at 0.65 μm (or $2/Q_{\text{ext}}(r_e/\lambda)$, used previously in Fig. 5). In order to implement the Nakajima and King algorithm, it is first necessary to compute the reflection function, plane al-

bedo, total transmission, and spherical albedo for the standard problem of plane-parallel homogeneous cloud layers (A_g) with various τ_c' and $r_e = 2^{(n+1)/4}$ for $n = 5, \dots, 19$, assuming a model cloud particle size distribution such as a log-normal size distribution. We have generated the reflection function libraries for $\tau_c' = 0.4, 0.8, 1.2$ and ∞ ($\tau_c = 3, 5, 8$ and ∞), fluxes libraries for $\tau_c' = 0.4, 0.8$, and 1.2 , and a

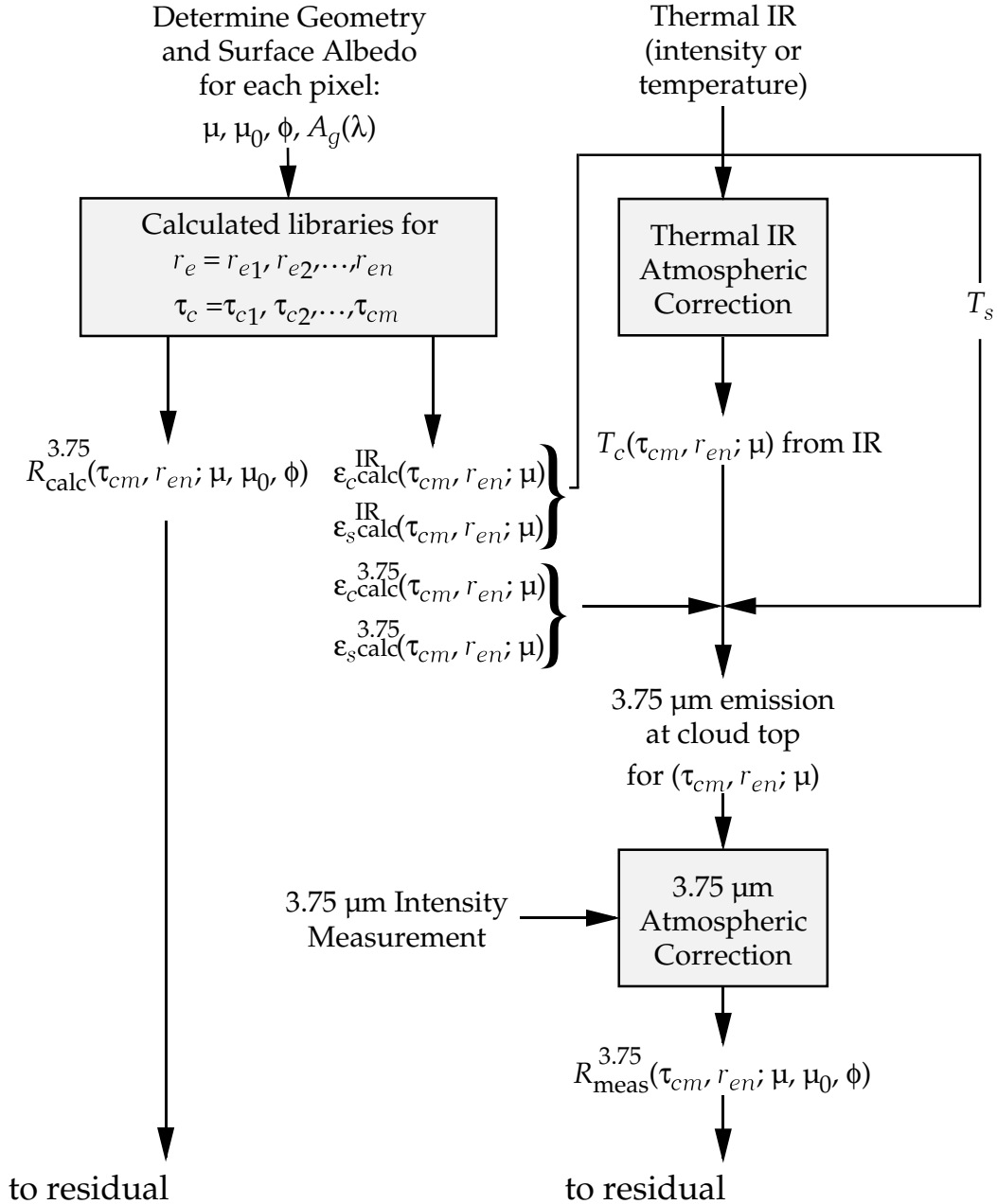


Figure 13. A general cloud retrieval algorithm for determining best fit for r_e and τ_c in the 3.75 μm band.

library for asymptotic functions and constants. These values of τ_c' are selected such that interpolation errors are everywhere $\leq 3\%$ for $\tau_c' \geq 0.6$ ($\tau_c \approx 4$). This was accomplished using a combination of asymptotic theory for $\tau_c' \geq 1.8$ ($\tau_c \approx 12$) and spline under tension interpolation for $\tau_c' < 1.8$.

The interpolation scheme reduces the number of library optical thickness entries substantially, but replaces those entries with a combination of spline interpolation and asymptotic formulae, depending on optical thickness. Calculations of the reflection function can be performed using the discrete ordinates method formulated by Nakajima and Tanaka (1986) or Stamnes et al. (1988). The asymptotic functions and constants that appear in Eqs. (7)–(9) can be obtained from solutions of an eigenvalue equation that arises in the discrete ordinates method (Nakajima and King 1992).

If one assumes that each reflection function measurement is made with equal relative precision, maximizing the probability that $R_{\text{meas}}^i(\mu, \mu_0, \phi)$ observations have the functional form $R_{\text{calc}}^i(\tau_c, r_e; \mu, \mu_0, \phi)$ is equivalent to minimizing the statistic χ^2 , defined as (Nakajima and King 1990)

$$\chi^2 = \sum_i \left[\ln R_{\text{meas}}^i(\mu, \mu_0, \phi) - \ln R_{\text{calc}}^i(\tau_c, r_e; \mu, \mu_0, \phi) \right]^2, \quad (17)$$

where the summation extends over all wavelengths λ_i for which measurements have been made and calculations performed.

Minimizing χ^2 as defined by Eq. (17) is equivalent to making an unweighted least-squares fit to the data (Bevington 1969). The minimum value of χ^2 can be determined by setting the partial derivatives of χ^2 with respect to each of the coefficients $[\tau_c(0.65 \text{ or } 0.75 \mu\text{m}), r_e]$ equal to zero. Due to the complicated dependence of the reflection function on τ_c and r_e , however, this solution is nonlinear in the unknowns τ_c and r_e such that no analytic solution for the coefficients exists.

Even for optically thick layers, where asymptotic theory applies, $R_{\infty}^i(r_e; \mu, \mu_0, \phi)$ is a complicated function of the phase function, and hence r_e , as King (1987) has shown by deriving the cloud optical thickness assuming the clouds had two different phase functions but the same asymmetry factor.

In order to solve this nonlinear least-squares problem, we have adopted a procedure whereby the scaled optical thickness τ_c' , and hence τ_c and g , is determined as a function of r_e from a reflection function measurement at 0.75 μm (or 0.65 μm for the case of MODIS data). For $\tau_c' < 1.8$ we used spline under tension interpolation (Cline 1974) of reflection function calculations $R_{\text{calc}}^i(\tau_c, r_e; \mu, \mu_0, \phi)$, and for $\tau_c' \geq 1.8$ we used Eq. (8), as described by King (1987). Having determined an array of possible solutions $[\tau_c, r_e]$, it is straightforward to calculate χ^2 as a function of r_e using measurements and calculations for one or more additional channels. Thus the determination of the optimum values of τ_c and r_e becomes a nonlinear least-squares problem in only one unknown r_e , since τ_c is given uniquely from a knowledge of r_e . The only subtlety worth noting is that it is essential to allow for the spectral dependence of $\tau_c(\lambda)$ and $A_g(\lambda)$ when interpolating radiative transfer calculations $[\tau_c'(\lambda) < 1.8]$ or applying Eq. (9) $[\tau_c'(\lambda) \geq 1.8]$ at channels other than 0.65 μm .

As an illustration of how this procedure works, Nakajima and King (1990) constructed the χ^2 hypersurface in coefficient space for various combinations of bands. These results, presented in Fig. 14, are based on simulated spherical albedo measurements at (a) 0.75 and 2.16 μm , (b) 0.75, 1.65 and 2.16 μm , (c) 0.75 and 3.70 μm , and (d) 0.75, 1.65, 2.16 and 3.70 μm . The solid curves represent constant values of χ^2 . The parameters τ_c and r_e that give the best fit of the measurements R_{meas}^i to the nonlinear function $R_{\text{calc}}^i(\tau_c, r_e)$ are determined by the location of the minimum value of χ^2 in this two-dimensional space. The results pre-

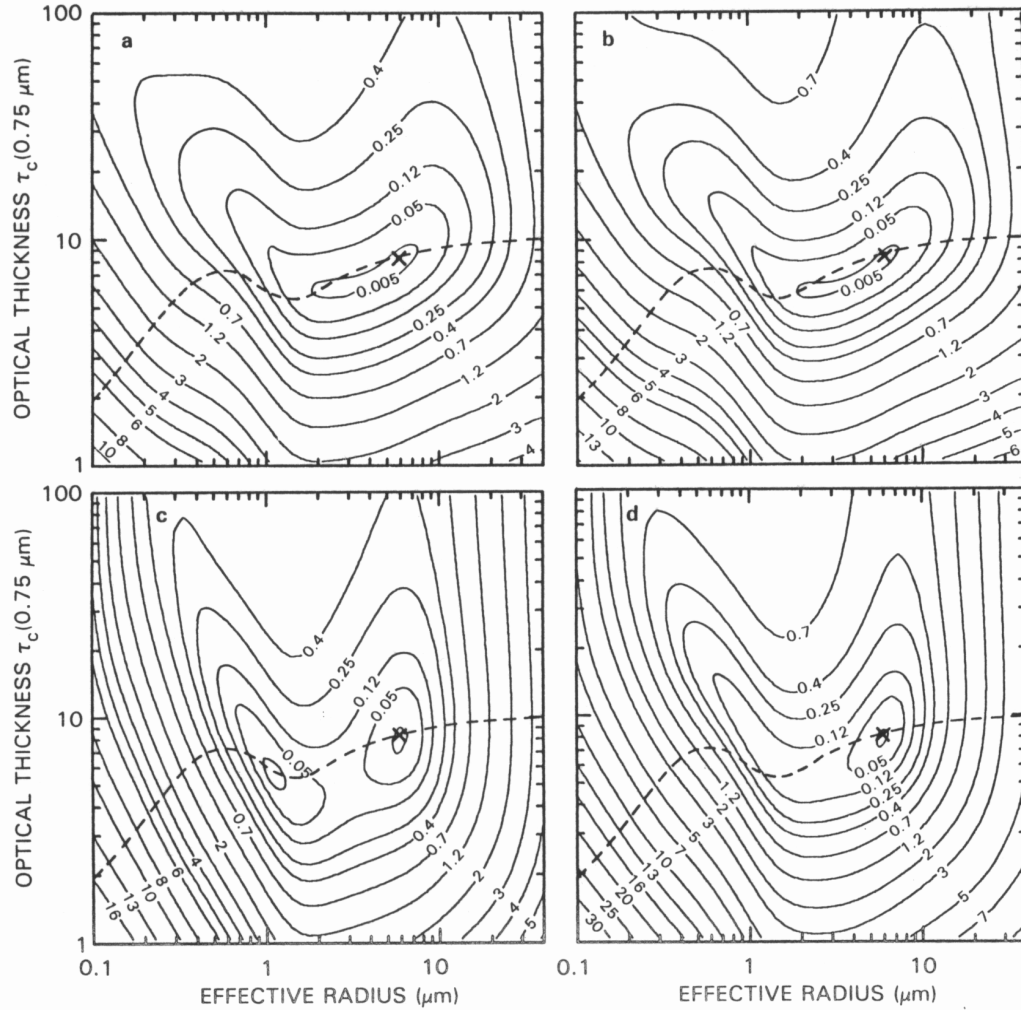


Figure 14. χ^2 hypersurface for theoretically generated spherical albedo measurements at (a) 0.75 and 2.16 μm , (b) 0.75, 1.65 and 2.16 μm , (c) 0.75 and 3.70 μm , and (d) 0.75, 1.65, 2.16 and 3.70 μm . The solid curves represent constant values of χ^2 , while the dashed curve in each panel represents the array of possible solutions for $R_{\text{meas}}^{\text{U/V}} = 0.495$. These results were constructed for a model cloud layer having $\tau_c(0.75 \mu\text{m}) = 8$ and $r_e = 6 \mu\text{m}$, located by the minimum value of χ^2 in this two-dimensional space [from Nakajima and King (1990)].

sented in Fig. 14 were constructed for the optimum values $\tau_c = 8$ and $r_e = 6 \mu\text{m}$. Searching this hypersurface for the parameters that minimize χ^2 is greatly facilitated by first solving for τ_c as a function of r_e using the reflection function measurement at 0.75 μm . These optical thickness values, shown in each panel of Fig. 14 as a dashed line, must necessarily pass through the absolute minimum of the function χ^2 (assuming no error in the visible measurement). The previously

mentioned multiple solutions are readily seen for small r_e and τ_c , though the ambiguity is eliminated in Fig. 14d when using all available near-infrared channels.

We are also exploring the possibility of retrieving τ_c and r_e separately using pairs of channels (e.g., 0.65 and 1.64 μm , 0.65 and 2.13 μm , and 0.65 and 3.75 μm) since each near-infrared absorbing channel is sensitive to the effective radius at a different depth within the cloud (Platnick 1996). The lowest (optical thickness-sensitive) channel will be either 0.65 μm over land, 0.86 μm over water, or 1.24 μm over snow and sea ice surfaces. For water clouds, the effective radius typically increases from cloud base to cloud top, with the 3.75 μm retrieval being the most sensitive to drops high in the cloud and 1.64 μm much lower in the cloud. For ice clouds, the vertical profile of effective radius is just the opposite, with the smallest crystals highest in the cloud. Although the χ^2 multichannel retrieval algorithm described above has the merit of eliminating multiple solutions, the effective radius thus obtained in realistic, vertically inhomogeneous clouds, is some compromise in effective radius. We are thus planning on doing multiple retrieval using the similarity (or differences) in the retrieved results as a quality control indicator in the output data product. If the differences between retrievals are excessively large (i.e., $\Delta r_e \gtrsim 2 \mu\text{m}$), then we will switch to an ice retrieval algorithm that is identical to the one outlined above, but with an ice crystal phase function rather than water droplet phase function in the look-up tables.

3.2. *Variance and uncertainty estimates*

The overall uncertainties in determining the cloud optical thickness and effective radius can loosely be categorized as originating in either the *model* used for developing the cloud reflection function and emittance libraries, or in the

physical uncertainties brought about through changing instrument error and atmospheric effects. Though it is difficult to draw the line between the two, it is convenient to consider the model uncertainties to have their source in the library generating algorithm shown schematically in Fig. 11 and the algorithm used for approximating emitted thermal radiation at $3.75\ \mu\text{m}$. The physical uncertainties can be largely ascribed to the atmospheric correction boxes and the measured data shown in Fig. 12.

3.2.1. *Model uncertainties*

Several sources of model error are potentially significant. First of all, the treatment of the wavelength integration over the bandpass filters is important because it impacts calculations of the spectral reflection functions and emissivities. Ideally, the spectral integration should be based on the variability of the optical constants across the bandpass filter. For example, the absorption of liquid water, as measured by the imaginary part of the complex refractive index of water, varies significantly throughout the near-infrared wavelength region, whereas the real part of the refractive index is approximately constant over this region. Mie calculations are dependent on the size parameter ($2\pi r/\lambda$), thereby adding another wavelength dependence. For computational reasons, it is desirable to determine the minimum number of wavelengths needed in any retrieval.

In order to assess the impact of finite bandpass characteristics of the MODIS bands on our cloud retrieval algorithm, we performed calculations of the reflection function using 11 equally-spaced wavelengths for each band. These results were then compared with reflection function computations based on a single wavelength at the bandpass center. Ultimately, however, it is the effect of the wavelength integration on the retrieval of τ_c and r_e that is important, not the absolute changes in the reflection functions themselves. Since the near-infrared re-

flection functions are more sensitive to the finite bandpass characteristics of MODIS, we restrict our analysis to the retrieval of r_e .

Figure 15 shows the error in the retrieval of r_e when using a single wavelength calculation for the 2.14 μm band of MAS, where the 11 wavelength integration over the bandpass characteristics of the band is taken as the “true solution.” The optical thickness is such that the asymptotic reflection function has been reached for most radii. This choice of optical thickness gives a conservative estimate of retrieval error since the sensitivity of r_e to reflection function is the

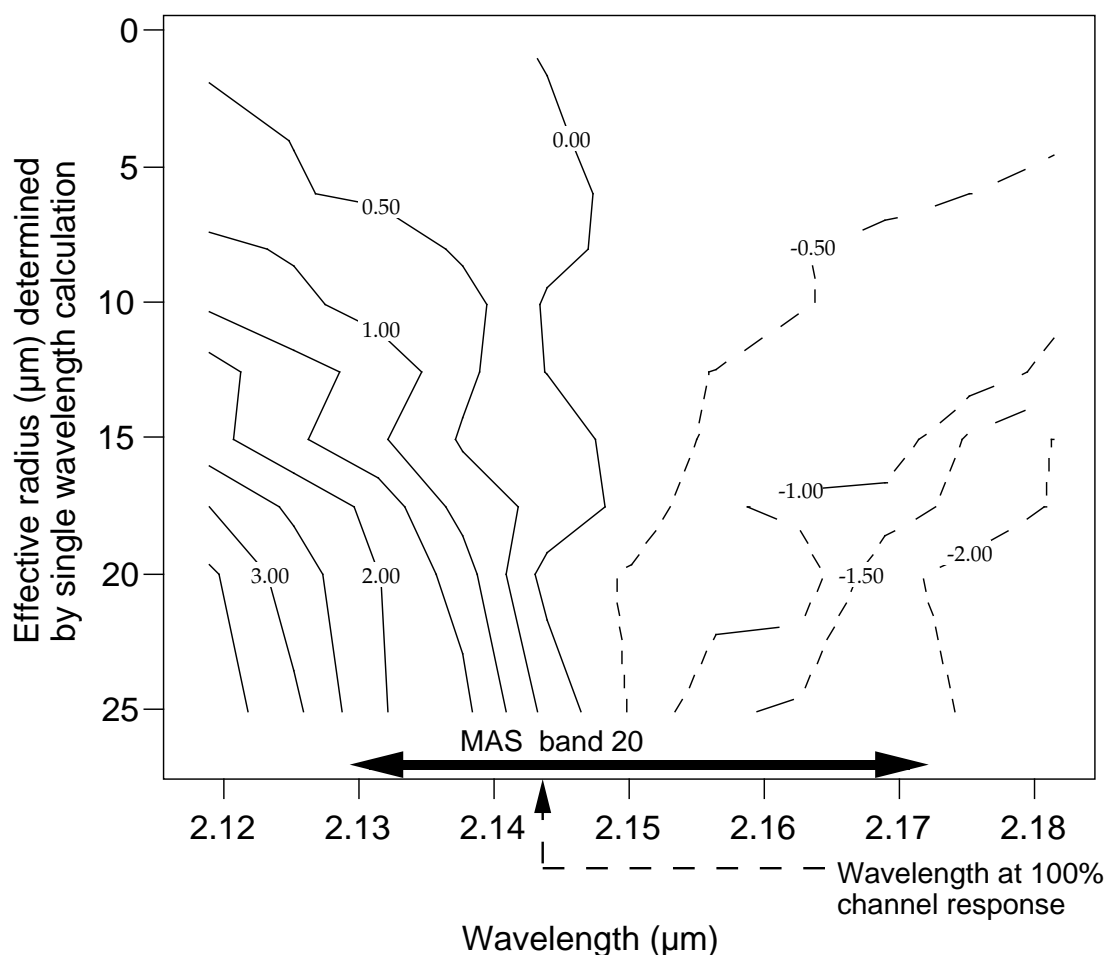


Figure 15. Error in the retrieval of r_e (μm) between (i) using spectrally averaged reflection functions, sensor and solar weighted with 11 wavelengths, and (ii) a single wavelength calculation. These results apply to the MAS 2.14 μm band with $\mu_0 = 0.75$, $\mu = 0.95$, $\tau_c = 50$, and the optical constants of Irvine and Pollack (1968).

smallest. Figure 15 shows that using the wavelength of the peak of the spectral bandpass is sufficient for obtaining effective radii errors within $0.5 \mu\text{m}$.

Another approach one might take is to spectrally integrate the optical parameters ω_0^λ , Q_{ext}^λ , and g^λ over wavelength and use these results for a single wavelength retrieval. This comparison is shown in Fig. 16 for the same MAS channel as shown in Fig. 15. For $\tau_c = 50$, the error is less than $0.1 \mu\text{m}$ for the expected range of effective radii to be encountered in terrestrial clouds. For an optically thin cloud ($\tau_c = 1$) the error increases to $0.3 \mu\text{m}$ at $r_e = 4 \mu\text{m}$. However, for such an optically thin cloud, uncertainties in surface reflectance and atmospheric

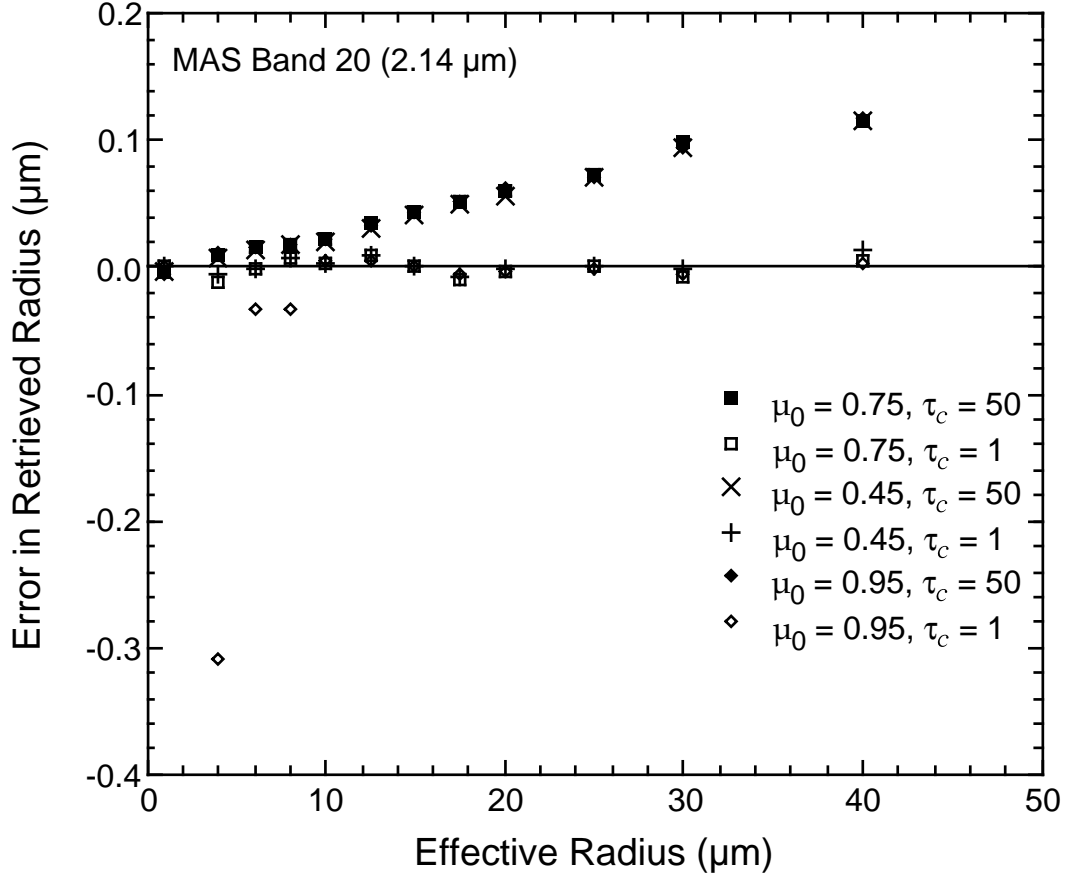


Figure 16. Error in the retrieval of r_e (μm) between (i) using spectrally averaged reflection functions, sensor and solar weighted with 11 wavelengths, and (ii) using reflection function calculations based on spectral averages of cloud optical properties (ω_0^λ , Q_{ext}^λ , and g^λ). These results were obtained using the MAS $2.14 \mu\text{m}$ band with $\mu = 0.95$ and the optical constants of Irvine and Pollack (1968).

corrections are likely to dominate this error. Similar results were obtained when analyzing MAS 1.62 and 3.73 μm bands. At this time, it appears that an integration over ω_0^λ , Q_{ext}^λ , and g^λ will provide an adequate reflectance library. Table 3 summarizes the maximum retrieval errors in r_e for all near-infrared bands (based on calculations at $\mu_0 = 0.95, 0.75, 0.5$, $\mu = 0.95$ and $\tau_c = 1, 5, 50$). Effects of spectral integration on emission in the 3.7 μm channels are not included in Table 3.

Table 3. Summary of approximate maximum error in retrieving effective radius (μm) for MAS near-infrared channels and AVHRR channel 3. Calculated for $\mu = 0.95$ and μ_0 variable. For the spectral and optical constant analysis, the two rows for each band correspond to the maximum error as r_e varies from 5 to 20 μm with τ_c variable. For the sensor error analysis, for each band correspond to different optical thicknesses and $5 \leq r_e \leq 15 \mu\text{m}$. See text for details.

Band	r_e	$\langle R^\lambda \rangle - R^{\text{Mie}}$	$+\lambda_c$ shift (+13% of BW)	$-\lambda_c$ shift (-13% of BW)	$r_e(\text{IP}) - r_e(\text{PW})^*$	τ_c	Errors due to sensor intensity or reflectance error			
							$\pm 1\%$	$\pm 2\%$	$\pm 5\%$	$\pm 10\%$
MAS 10 (1.62 μm)	5	+0.09	-0.10	+0.10	+0.5	5	∓ 0.7	∓ 1.3	-3/+4	+6/+9
	20	-0.05	-0.55	+0.55	+3.0	50	∓ 0.7	∓ 1.3	∓ 2.7	-4.5/+6
MAS 20 (2.14 μm)	5	+0.10	-0.15	+0.15	+0.5	5	∓ 0.4	∓ 0.7	∓ 2.0	-3.5/+4.5
	20	-0.30	-0.50	+0.50	+2.6	50	∓ 0.3	∓ 0.6	∓ 1.4	∓ 2.7
MAS 32 [†] (3.73 μm)	5	+0.25	-0.30	+0.30		5	∓ 0.15	∓ 0.2	∓ 0.6	∓ 1.2
	20	-0.05	-0.70	+0.70		50	∓ 0.2	∓ 0.3	∓ 0.7	-1.4/+1.7
AVHRR 3 (3.75 μm)	5	+0.45	-0.30	+0.50		5	Same as for MAS 32			
	20	-0.10	-0.70	+1.20		50				

* Difference in retrieved droplet effective radius using reflectance libraries calculated with the optical constants given by IP (Irvine and Pollack 1968) and PW (Palmer and Williams 1974). These computations apply to the case when $\tau_c = 50$.

[†] Designated as MAS 31 prior to June 1996.

The effect of a shift in the central wavelength of the near-infrared bands can also be assessed. For each band, the reflection function changes arising from a shift of 13% in the bandpass center were compared with those based on spectral integration over the full-width half maximum (FWHM) bandpass of each band (one wavelength increment in the 11 wavelength calculation). Such a spectral shift is approximately equal to the tolerance listed in the MODIS specifications. The effect of a spectral shift on the retrieval of r_e is shown in Fig. 17 for the MAS 2.14 μm band. In general, the error increases with increasing r_e , but for $r_e < 20 \mu\text{m}$ the error $\Delta r_e < 0.5 \mu\text{m}$. Table 3 summarizes errors in r_e arising from spectral shifts in other near-infrared channels of MAS and AVHRR. The effect of spectral shift on emission is not included in Table 3 for either the MAS or AVHRR 3.7 μm channels.

The optical constants of liquid water are the starting point for all calculations. The optical constants of water in various near-infrared spectral regions are reported in the compilation papers of Irvine and Pollack (1968) and Hale and Querry (1973), and the measurements of Robertson and Williams (1971), Palmer and Williams (1974), Downing and Williams (1975), and Kou et al. (1993). All constants were derived for water at room temperature, with the exception of Kou et al. who also made measurements of supercooled water at -8°C . For the 3.7 μm band, the data of Downing and William and Kou et al. agree quite well with those of Irvine and Pollack. In the 1.64 and 2.13 μm channels, on the other hand, differences of up to 11-14% occur between the absorption coefficient of liquid water reported by Irvine and Pollack and corresponding measurements reported by Palmer and Williams, depending on wavelength. The room temperature absorption measurements of Kou et al. are within a few percent of Palmer and Williams. However, absorption bands for their supercooled measurements are

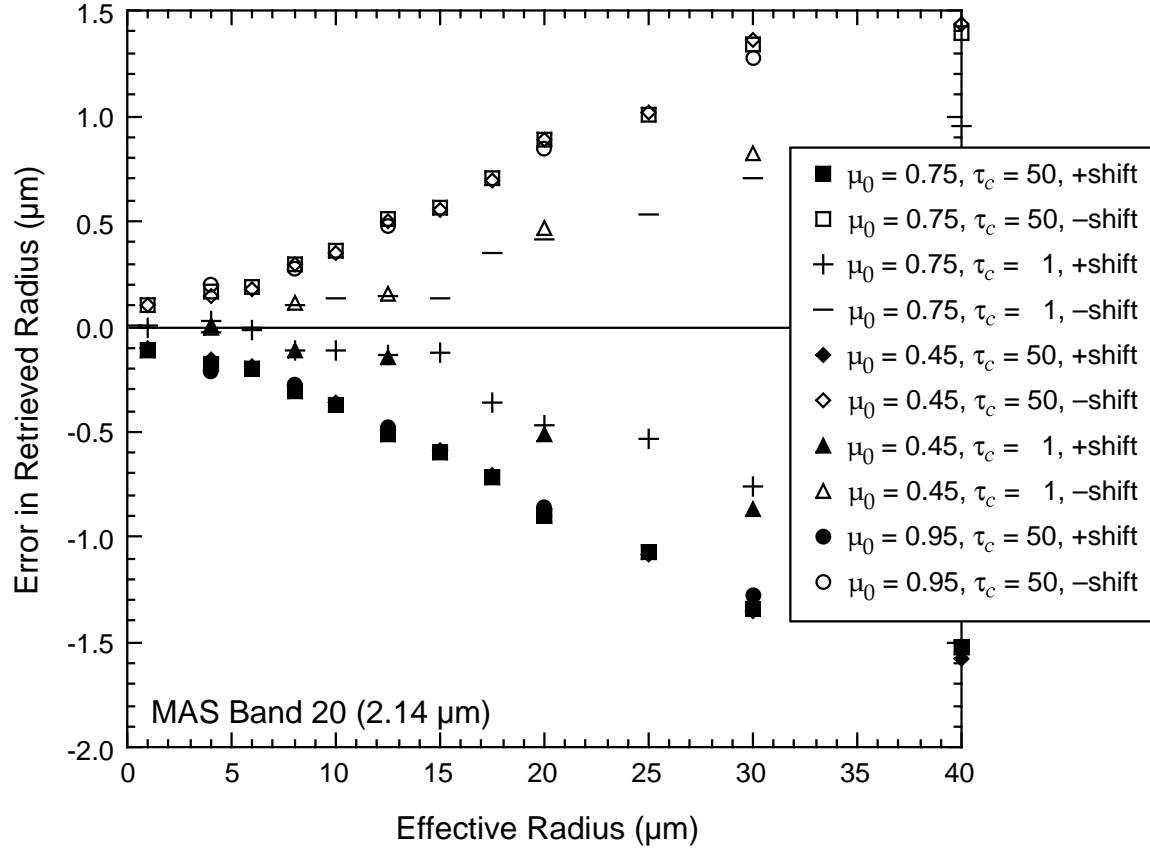


Figure 17. Error in the retrieval of r_e (μm) between (i) using spectrally averaged reflection functions, sensor and solar weighted with 11 wavelengths, and (ii) using reflection function calculations with a spectral shift of 13% (± 6.25 nm) in the band's central wavelength. These results were obtained using the MAS 2.14 μm band with $\mu = 0.95$ and the optical constants of Irvine and Pollack (1968).

slightly shifted toward longer wavelengths giving an increase in absorption over the room temperature values by about 20% at the center of the MODIS 1.64 μm channel, and 5% for the 2.13 μm channel.

At large cloud optical thicknesses, it can be shown that the fractional effective radius retrieval error is approximately equal, but of opposite sign, to the fractional error in the absorption constant (Platnick and Valero 1995). That is, a library calculated using an absorption constant that is 10% too small would result in a retrieved effective radius that is about 10% too large. Exact calculations of the effects of different absorption coefficients on the retrievals of r_e are shown in Fig. 18 for the 1.62 and 2.14 μm bands of MAS, using both Irvine and Pollack

(1968) and Palmer and Williams (1974) data. These results were obtained for several values of optical thickness and solar zenith angle. Note that the fractional effective radius retrieval error is indeed approximately constant with effective radius for the larger optical thicknesses, as mentioned above. A supercooled water cloud (Kou et al. 1993) would show even greater differences. Since it is difficult to know which authors have presented the more accurate liquid water absorption values, the example of Fig. 18 should be regarded as a fundamental un-

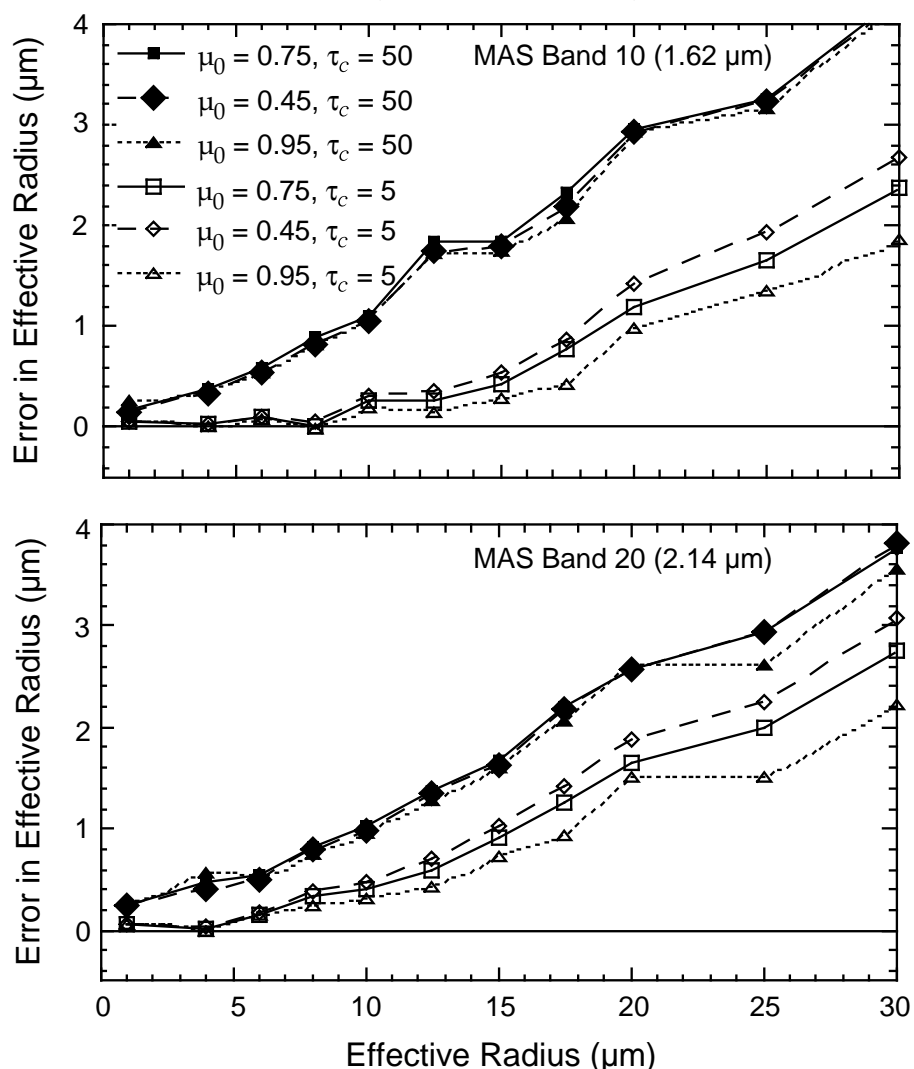


Figure 18. Error in the retrieval of r_e (μm) between using spectrally averaged reflection function calculations based on liquid water optical constants (i) reported by Irvine and Pollack (1968) and (ii) measured by Palmer and Williams (1973). These results were obtained with $\mu = 0.95$ for the MAS 1.62 μm band (top) and the MAS 2.14 μm band (bottom).

certainty in the retrieval of effective radius. For computing the libraries of Fig. 11, we have chosen to use the optical constants of Palmer and Williams (1974) for the 1.64 μm MODIS channel, and Downing and Williams (1975) for the 2.13 μm and greater channels. For visible channels below 0.69 μm , we have used the optical constants tabulated by Hale and Querry (1973).

While this model uncertainty arises from an inadequate knowledge of two physical quantities, those quantities are fixed; it is accurate data that are lacking. The same can be said of the extraterrestrial solar flux needed to calculate the reflection function from calibrated intensity observations.

3.2.2. *Physical uncertainties*

Physical uncertainties arise due to *changing* physical quantities, such as changes in the above cloud atmosphere (i.e., aerosol loading, thin cirrus, water vapor, molecular scattering) and instrument calibration changes. These examples affect, respectively, the signal received at the satellite and its subsequent value as interpreted by the instrument. Both can be lumped together and ascribed to an overall error in determining the cloud reflection function at wavelength λ_i (ΔR_{meas}^i).

Due to the multiwavelength nature of our cloud retrieval algorithm, together with the near orthogonality of the retrieval of τ_c and r_e (cf. Fig. 9), it is useful to examine the errors in τ_c arising from uncertainties in the visible reflectance, and errors in r_e arising from uncertainties in the near-infrared reflectance. Figure 15 presents an analysis of errors in r_e due to a 1, 2, 5, or 10% error in the reflection function in the near-infrared for MAS ($\Delta R_{\text{meas}}^{2.14}$). Calibration errors are expected to be within 2% for the MODIS 0.65, 1.64 and 2.13 μm bands. Atmospheric transmission to cloud top, direct plus diffuse, is likely to be about 90-95% for

most bands, causing a minimum of about a 10% reduction in solar reflected signal if no atmospheric correction is taken into account (round trip transmission $\approx 0.95^2 \approx 0.9$). Variability in this transmission, atmospheric emission in the $3.75 \mu\text{m}$ band, and the effect of aerosol on atmospheric scattering in the visible further complicate this analysis. Considering the near-infrared channels alone, if our ability to account for this variability is limited to 10%, then Fig. 19 suggests that we can only expect that our uncertainty Δr_e is within $1\text{--}3 \mu\text{m}$ for optically thick clouds (depending on the band used). This analysis, summarized in Table 3, is limited to a few solar and observational geometries and optical thicknesses, and

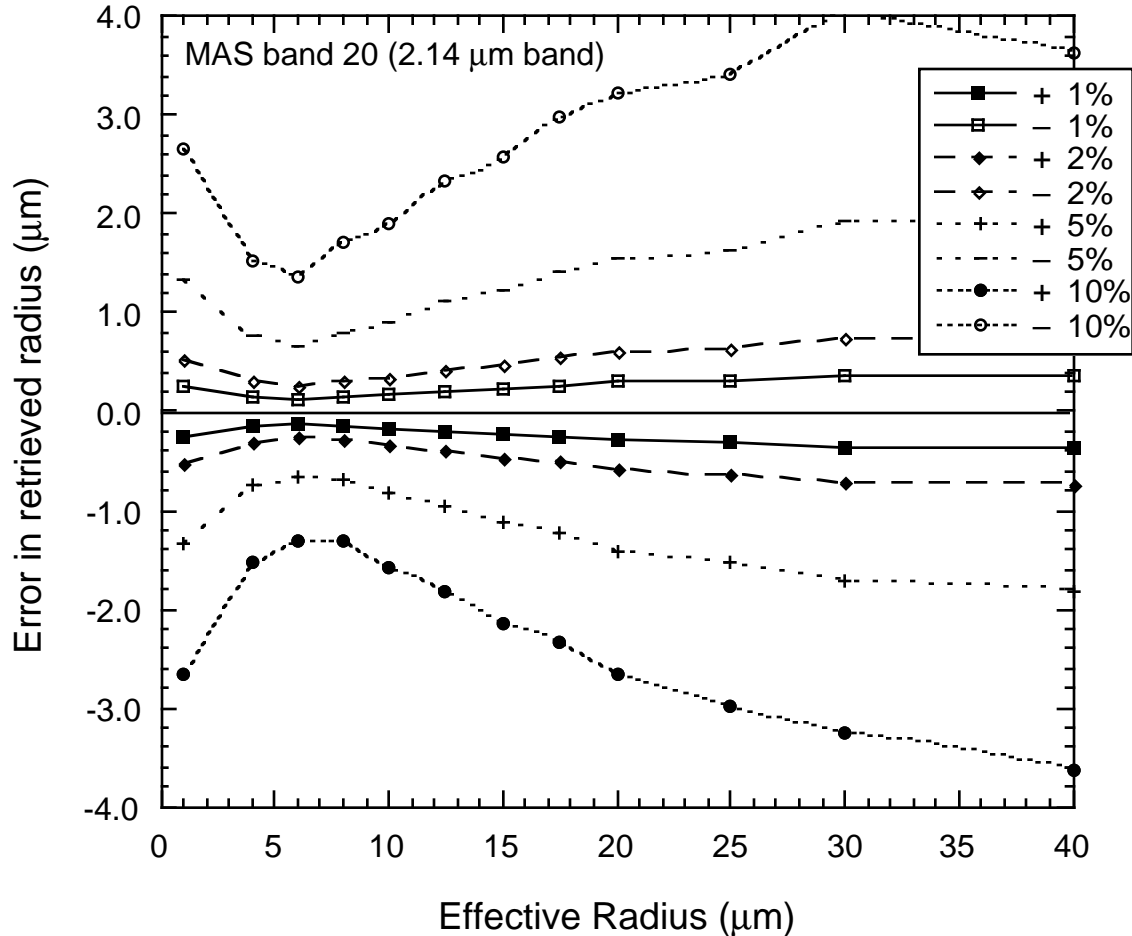


Figure 19. Error in the retrieval of r_e (μm) between (i) using spectrally averaged reflection functions, sensor and solar weighted with 11 wavelengths, and (ii) reflection function measurements assuming an error of $\pm 1, 2, 5$, and 10% . These results were obtained using the MAS $2.14 \mu\text{m}$ band with $\mu_0 = 0.75$, $\mu = 0.95$, $\tau_c = 50$, and the optical constants of Irvine and Pollack (1968).

thus there is no certainty that errors in excess of these estimates might not sometimes arise.

Determining the effect of atmospheric variability on the retrieval of cloud optical and microphysical properties is an important aspect of ongoing research. Additional sources of model error being investigated include the effects of the size distribution (i.e., effective variance) and in-cloud water vapor absorption.

The previous analysis was for errors in the near-infrared reflection function only. To assess the overall uncertainties in the retrieved optical thickness and effective radius, Nakajima and King (1990) performed radiative transfer computations at 0.75, 1.65 and 2.16 μm . At each wavelength the reflection function was computed for $\theta_0 = 10, 60^\circ$, $\theta = 0, 10, 30, 50^\circ$, $\phi = 0, 10, 30, 60, 120, 150, 170, 180^\circ$, $\tau_c = 4, 8, 16, 32$ and $r_e = 4, 8, 16 \mu\text{m}$.

After confirming that the algorithm returns the correct values of τ_c and r_e for simulated measurements with no observational error, they introduced observational error of 5% into the reflection function at one channel, with no observational error in either of the other two channels.

The results of these simulations are presented in Fig. 20, which shows the relationship between errors in r_e and τ_c for 5% error in the reflection function at 0.75 μm (solid circles), 1.65 μm (open squares) and 2.16 μm (solid triangles). While there are instances for which the error in τ_c is large when the error in r_e is negligible, the overall tendency of these simulations is for an error in τ_c to occur whenever there is an error in r_e . The former condition corresponds to the situation in which the optical thickness is large and measurement (or calibration) errors are confined solely to 0.75 μm . The latter condition, on the other hand, occurs primarily when measurement errors occur at 1.65 or 2.16 μm with no corresponding errors at 0.75 μm . The relationship between errors in τ_c and r_e may be

understood as follows. For optically thick layers the reflection function at a nonabsorbing wavelength is primarily a function of the scaled optical thickness, and thus the scaled optical thickness retrieved by our analysis is nearly independent of particle radius. Thus,

$$\frac{\partial \ln \tau_c'}{\partial \ln r_e} = \frac{\partial \ln(1-g)}{\partial \ln r_e} + \frac{\partial \ln \tau_c}{\partial \ln r_e} \approx 0. \quad (18)$$

From computations of the asymmetry factor as a function of effective radius (Table 4), it follows that at $0.75 \mu\text{m}$,

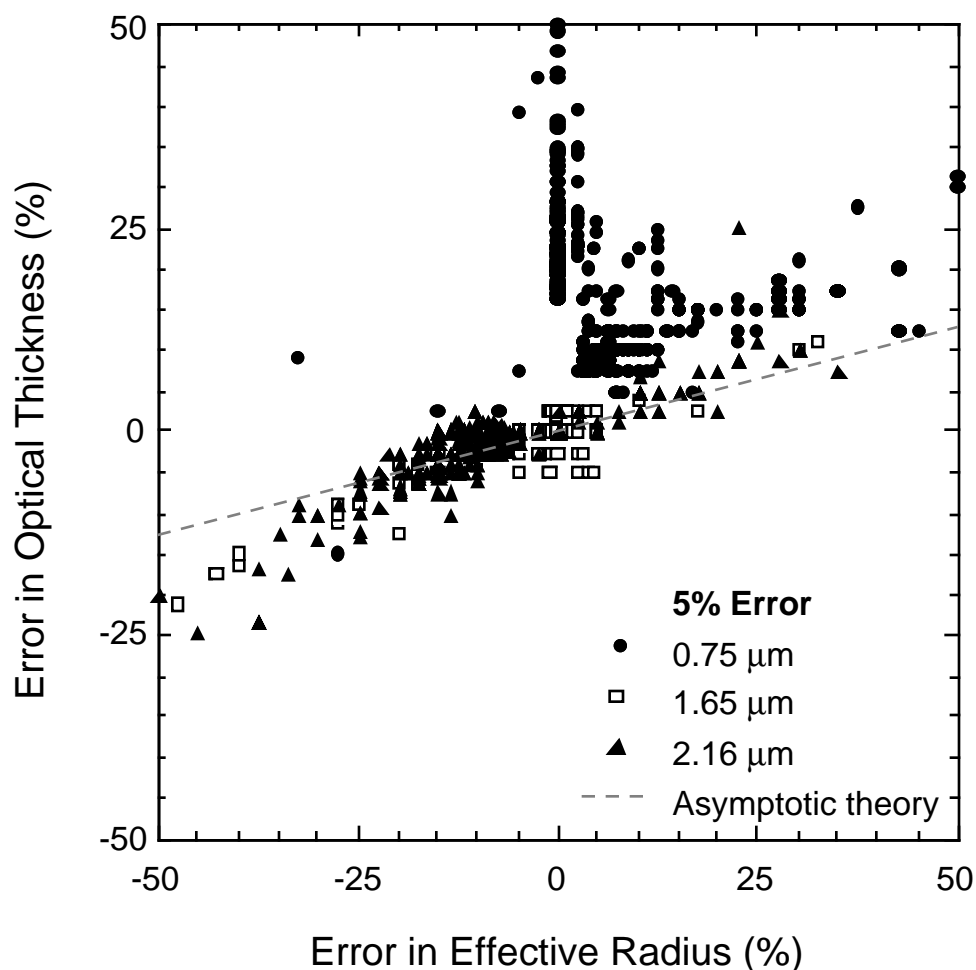


Figure 20. Simultaneous errors in the retrieved optical thickness and effective radius for simulations containing 5% error in the reflection function at $0.75 \mu\text{m}$ (solid circles), $1.65 \mu\text{m}$ (open squares), or $2.16 \mu\text{m}$ (solid triangles). The dashed curve superimposed on these results is the error predicted by Eq. (20) (see text for details) [from Nakajima and King (1990)].

TABLE 4. Optical properties of the cloud droplet polydispersions used in the numerical simulations.*

r_e	$\lambda = 0.75 \mu\text{m}$	$\lambda = 2.16 \mu\text{m}$			$\lambda = 3.70 \mu\text{m}$		
	$m = 1.332 - 0.0i$	$m = 1.294 - 0.00035i$			$m = 1.374 - 0.0036i$		
	g	ω_0	g	k	ω_0	g	k
2.13	0.782	0.99708	0.853	0.0360	0.9783	0.790	0.119
3.00	0.812	0.99578	0.836	0.0458	0.9747	0.802	0.125
4.25	0.832	0.99288	0.803	0.0652	0.9627	0.783	0.160
6.00	0.846	0.98880	0.801	0.0824	0.9387	0.756	0.217
8.50	0.856	0.98408	0.828	0.0917	0.9099	0.775	0.256
12.00	0.862	0.97786	0.850	0.1019	0.8811	0.819	0.275
17.00	0.867	0.96949	0.863	0.1160	0.8465	0.850	0.302
24.00	0.870	0.95849	0.874	0.1321	0.8045	0.872	0.336
34.00	0.873	0.94398	0.885	0.1508	0.7558	0.893	0.375

* All computations were performed assuming a log-normal size distribution with $\sigma = 0.35$ ($v_e = 0.13$).

$$\frac{\partial \ln(1-g)}{\partial \ln r_e} \simeq -0.50 + 0.15 \ln r_e. \quad (19)$$

In the radius range $4 \lesssim r_e \lesssim 6 \mu\text{m}$, where the error in effective radius is especially large, a combination of Eqs. (18) and (19) leads to

$$\frac{\partial \ln \tau_c}{\partial \ln r_e} \simeq 0.26. \quad (20)$$

This result, shown in Fig. 20 as a dashed line, is seen to be a reasonable approximation for $|\Delta r_e / r_e| \lesssim 25\%$ and for cases in which the measurement error is confined largely to 1.65 or 2.16 μm . The large errors in droplet radius, which are generally associated with errors in excess of those predicted by Eq. (20), arise primarily when τ_c and r_e are small, cases for which asymptotic theory and the assumption of Eq. (18) are no longer valid. In a one channel method for determining the cloud optical thickness (cf. King 1987, Rossow et al. 1989), where it is necessary to assume a value of r_e , Fig. 20 suggests that errors of $\pm 25\%$ can arise in the optical thickness for errors of $\pm 50\%$ in effective radius.

3.3. *Practical considerations*

3.3.1. *Numerical computation considerations*

a. Parameter description

Our group is currently committed to producing three parameters as part of MODIS product MOD06 (*Cloud Product*). Parameter 1780 (*Effective Particle Radius*) has units of μm (10^{-4} cm), and ranges from 0 to 100. Parameter 2311 (*Cloud Optical Thickness*) is dimensionless, and ranges from 0 to 100. Parameter 1764 (*Cloud Particle Phase*) has seven states. Code values from 0 to 6 have the following translation: 0–clear, 1–opaque water cloud, 2–opaque ice cloud, 3–mixed phase cloud, 4–non-opaque ice cloud, 5–non-opaque water cloud, and 6–uncertain. The *Cloud Particle Phase* is a post-launch parameter.

b. Data storage estimates

The following storage estimates are based on a 1 km resolution at nadir. The MODIS Science Data Support Team (SDST) estimates 8×10^8 pixels per day for level-1B 1 km pixels, including day and night.

Parameter 1764 (*Cloud Particle Phase*) requires 3 bits of data storage (0-6). This parameter will be derived for each 1 km pixel over the entire globe during the daytime. Thus the data storage required per day, separate from the needs of the Menzel and Strabala infrared algorithm (ATBD-MOD-04), is approximately

$$\begin{aligned} (4 \times 10^8 \text{ pixels}) \times 3 \text{ bits/pixel} &= 1.2 \times 10^9 \text{ bits} \\ &= 143.1 \text{ Mbytes.} \end{aligned}$$

Parameter 1780 (*Effective Particle Radius*) has values ranging from 0 to 100. One decimal place provides adequate precision. Thus the values will be scaled up by a factor of 10 and stored as 10 bit integers. This parameter will be derived for each cloudy 1 km pixel over the entire globe once per day (day time only). Thus the data storage required per day is approximately

$$\begin{aligned}
 (4 \times 10^8 \text{ pixels}) \times 10 \text{ bits/pixel} &= 4 \times 10^9 \text{ bits} \\
 &= 476.8 \text{ Mbytes.}
 \end{aligned}$$

Parameter 2311 (*Cloud Optical Thickness*) has values ranging from 0 to 100. One decimal place provides adequate precision. Thus the values will be scaled up by a factor of 10 and stored as 10 bit integers. This parameter will be derived for each cloudy 1 km pixel over the entire globe once per day (day time only). Thus the data storage required per day is approximately

$$\begin{aligned}
 (4 \times 10^8 \text{ pixels}) \times 10 \text{ bits/pixel} &= 4 \times 10^9 \text{ bits} \\
 &= 476.8 \text{ Mbytes.}
 \end{aligned}$$

Output will also have confidence levels assigned to retrieved particle size and optical thickness. This value ranges from -100 to 100. Using 11 bits per retrieval for confidence assignment adds another 524.5 Mbytes per day.

Thus the total storage required for parameters 1764, 1780, and 2311 per day is approximately

$$143.1 \text{ Mbytes} + 524.5 \text{ Mbytes} + 2 \times 476.8 \text{ Mbytes} = 1.62 \text{ Gbytes}$$

The daily data storage of level-2 data can easily be reduced by saving only those data that correspond to cloudy pixels (perhaps 60% of the globe), and by using data compression. We have not made any of those assumptions in these calculations, assuming that the entire global data set will be saved (as is the case for the ocean data sets, for example).

c. *Data processing requirements*

The efficient processing speed of the cloud retrieval code has been improved by about a factor of 6 since the β version of the code was first delivered. With the delivered version 1 code, the MODIS Science Data Support Team (SDST) estimated that it requires about 222 MFLOPS to generate parameters 1780 (*Cloud Effective Particle Radius*) and 2311 (*Cloud Optical Thickness*) with confidence level

values for daily observations over the entire globe (day time only). This includes a factor of 1.6 for additional time needed for data production, a factor of 0.4 for cloudy scenes, and a factor of 2 for atmospheric corrections.

Parameter 1764 (*Cloud Particle Phase*) is a post-launch product. The required data processing speed is not available at this time, since no prototype code has yet been developed. However, we estimate that, based on some of our research code, about 20 MFLOPS should be sufficient.

d. Required input data

Parameter 1764 (*Cloud Particle Phase*) requires product MOD02 (Level-1B Radiance, Calibrated) and product MOD03 (Geolocation Fields) as input data (cf. Fig. 1). Parameters 1780 (*Cloud Effective Particle Radius*) and 2311 (*Cloud Optical Thickness*) require the following input data:

Product MOD02 (Level-1B Radiance, Calibrated);

Product MOD03 (Geolocation Fields);

Product MOD35 (Cloud Mask);

Product MOD07 (Temperature and Moisture Profiles) and/or Product MOD05 (Precipitable Water Product);

Product MOD43 (BRDF/Albedo);

Product MOD06 (Cloud Product, parameter Cloud Top Properties and Cloud Phase);

Product MOD28 (Sea Surface Temperature);

Product MOD11 (Land Surface Temperature).

In addition, ancillary information on temperature and moisture profiles from NCEP gridded analysis is also required. This is not a unique requirement for these data products, and is required by many other investigators both within MODIS and for other science teams on the AM spacecraft. In the post-launch pe-

riod, the MODIS aerosol product MOD04 will also be useful for studying aerosol-cloud interactions and their effects on cloud retrievals.

Finally, to make our multichannel algorithm work the most efficiently, the MODIS SDST is running a preprocessor to provide all of our input channels at effective 1 km spatial resolution, based on integrating the 250 and 500 m pixels according to the point spread function of the MODIS instrument. This both reduces the data volume for the input and permits more ready access to our multichannel algorithm.

e. Level-3 gridded cloud data

The Level-3 Atmosphere Joint Product (MOD08) will be produced on a daily, 8-day and monthly time scale, each of which will be produced at both an equal angle ($0.5^\circ \times 0.5^\circ$) and equal area (~ 500 km) spatial scale (cf. Fig. 1). At the moment, we are planning to archive the following parameters from our cloud retrieval algorithm for each of these time and space scales: (i) histogram of cloud optical thickness for all water cloud pixels (100 bins), (ii) histogram of effective radius for all water cloud pixels (100 sizes), (iii) histogram of liquid water path for all water cloud pixels (100 sizes), derived as $W = 2\rho\tau_e r_e / 3$, where ρ is the density of water (1 g cm^{-3}), (iv) fraction of pixels in the grid box that were identified as water clouds and analyzed into the above histograms, (v) histogram of cloud optical thickness for all ice cloud pixels (100 bins), (vi) histogram of effective diameter for all ice cloud pixels (100 sizes), (vii) histogram of ice water path for all ice cloud pixels (100 sizes), and (viii) fraction of pixels in grid box that were identified as ice clouds and analyzed into the above histograms.

We have yet to design our integrated level-3 algorithm, which will combine parameters from multiple MODIS atmosphere products. Additional cloud pa-

rameters will be produced by Menzel and Strabala's algorithm (ATBD-MOD-04), and will be used to generate additional cloud histograms over the grid box (e.g., cloud top temperature, cloud top pressure).

We have not yet determined the best way to categorize the various quality control indicators into our joint level-3 product. This will be very important to our ability to diagnose global indicators of algorithm strengths and weaknesses. Once the combined MODIS level-3 product is defined and an algorithm developed, we will produce a separate ATBD that describes the joint level-3 atmosphere algorithm for MODIS.

3.3.2. *Validation*

Products from the present algorithm have been tested using MCR data (Nakajima et al. 1991) as well as from ongoing research projects that utilize MAS data, as described in Section 2.2. Several field programs offer opportunities for pre-launch and post-launch MODIS validation through collection and analysis of observations obtained from the MODIS Airborne Simulator (MAS; King et al. 1996) and High-spectral resolution Interferometer Sounder (HIS; Revercomb et al. 1988). These field campaigns, principal focus, and MODIS atmosphere group participants, include:

<i>Mission</i>	<i>Dates</i>	<i>Responsible Team Members</i>	<i>Primary Purpose</i>
FIRE III	April-June 1998	Michael King,	arctic stratus clouds
	Aug-Sep 1998	Si-Chee Tsay	over sea ice
LBA	September 1999	Bo-Cai Gao, Paul Menzel, Michael King, Si-Chee Tsay	tropical clouds and biomass burning
<i>MODIS-specific validation campaigns</i>			
California	July 1999	Michael King,	marine stratocumulus
	December 1999	Steve Platnick, Si-Chee Tsay	and valley fog

In addition to these ER-2 field campaigns, which often include the Cloud Lidar System (CLS; Spinhirne et al. 1989) for verifying cloud top altitude and multi-layer clouds, the University of Washington CV-580, with the Cloud Absorption Radiometer (CAR; King et al. 1986) and extensive in situ cloud microphysics (liquid water content, effective radius, cloud drop size distribution), aerosol properties (size distribution, scattering and absorption coefficients), and meteorological sensors, will be used as required.

In addition to these airborne campaigns in which we directly intend to participate, we expect to make use of selected ground-based networks as follows:

<i>Measurement</i>	<i>Location</i>	<i>Responsible Team Members</i>	<i>Primary Purpose</i>
ARM	Oklahoma, North Slope of Alaska, Western Tropical Pacific	Paul Menzel, Si-Chee Tsay	cloud base height (micropulse lidar), tem- perature and moisture profiles, sky radiance

The ground-based measurements will be obtained on a continuous basis as well as during intensive field experiments. All of these validation opportunities, as well as intercomparison of data derived from MODIS with other sensors on AM-1 and other spacecraft, will be discussed in detail below.

Validation will be approached in several ways: (i) collocation with higher resolution aircraft data, (ii) ground-based and aircraft in situ observations, and (iii) intercomparisons with other AM-1 platform instruments. Our validation approach relies heavily on the sources of the data that were used in the algorithm development, which consisted primarily of the MAS, HIS, and AVIRIS, a 224 band imaging spectrometer from 0.4–2.5 μm with 20 m resolution at nadir (Vane et al. 1993).

Since the spatial resolution of the MAS data is much smaller than that of MODIS, we are planning to use various types of spatial resolution data, such as

NOAA AVHRR and degraded MAS data, to test the algorithm during the pre-launch stage. In particular, we will use the recently upgraded MAS 50 channel 12 bit data, together with cloud mask information from Ackerman et al.'s algorithm (ATBD-MOD-06), to test our cloud retrieval algorithm.

In the first two years following the launch of EOS AM-1 (June 1998), we anticipate collecting data sets for the purpose of validating MODIS algorithms and data products through direct intercomparisons of MODIS data with in situ and airborne remote sensing data sets. A planned field activity that we envision participating in includes:

<i>Field Campaign</i>	<i>Principal Sensors</i>	<i>Responsible Team Members</i>	<i>Primary Purpose</i>
FIRE III	MAS, CLS, HIS, AirMISR, RAMS, in situ micro-physics	Michael King, Si-Chee Tsay, Steve Ackerman, Paul Menzel	arctic stratus clouds over sea ice

The first field campaign after the MODIS launch will be phase II of the FIRE III Arctic Stratus experiment described above. This component of FIRE III will be conducted 3-21 September 1998, and will coordinate the NASA ER-2 at high altitude (20 km), the NCAR C-130Q at low altitudes (1-6 km), and the SHEBA ice breaker ship, to be located near 77°N, 135°W in the Beaufort Sea. The ER-2 aircraft complement of sensors will include the MAS, CLS, RAMS (flux sensors), and the MISR airborne simulator, currently under development. By having MODIS, MISR, AIRS, and GLAS airborne simulators, as well as flux radiometers that will enable verification of CERES flux data sets from ER-2 altitudes as well as from the surface (SHEBA), this focused experiment should prove invaluable for intercomparison of MODIS-derived cloud mask and cloud products, CERES energy budget products, MISR multi-angle imagery, and in situ, surface and high altitude remote sensing observations.

Additional post-launch EOS-targeted field campaigns are discussed in the accompanying MODIS Atmospheres Validation Plan. During the post-launch stage, it is anticipated that one full day of MODIS data at the 1 km pixel resolution per week will be sufficient for algorithm testing and validation purposes. We only require the spectral channels used in our algorithm, but would also be interested in selected thermal channels to test our cloud screening algorithm. When a major algorithm revision is made, we will require a large data set to test and validate the algorithm. One month of MODIS level-1B data (for the channels given in Table 1) every 3 months (once per season) will be sufficient for this purpose.

Algorithm changes will be restrained to occur once per year as needed. We anticipate assessing the performance of the MODIS algorithms initially by processing one month per season (October, January, April, July), as well as specific time periods with validation experiments of special relevance, as outlined above. After initially looking at one year's data, consistency checks, quality assurance flags, validation campaigns, as appropriate, and intercomparisons with other instruments (especially on AM-1), we will begin whole-scale reprocessing, including every month. This initial stage may take in excess of one year, during which time the MODIS calibration algorithm will likely undergo additional refinement. Continual refinement of the MODIS "operational" algorithms will largely be conducted at the Team Members SCF as well as at the Team Leader Computing Facility (TLCF), as many of the algorithms are dependent on results from other algorithms (like calibration). Only periodically (after say 1.5 years following launch), the first reprocessing at the DAAC will be initiated.

3.3.3. *Quality control, diagnostics, and exception handling*

The quality control and diagnostics of all post-launch products will be performed based on comparisons with field programs in which related *in situ* cloud microphysical data are available. This type of exercise may provide some insights into refining the algorithm. Special cases of missing data, extremely low sun angles, and the presence of sun glint will be handled separately.

4. *Constraints, limitations, and assumptions*

There are several assumptions involved in the theoretical development of cloud particle size and optical thickness retrievals. At the present time, the algorithm is valid for single-layer, liquid water, plane-parallel geometry. Cloudy pixels that encounter multiple-layer and horizontal inhomogeneity will not be retrieved correctly. Further developments in the area of detecting multilayer cloud systems and of correcting for geometrical effects are needed. Also, some errors are expected to be encountered in retrieved cloud effective particle radius and optical thickness when ice clouds are present. We currently envision a switch (outlined above) for processing data using a Mie theory phase function for water clouds and an ice crystal phase function derived for hexagonal crystals for ice clouds (cf. Fig. 8). Finally, we have yet to determine the upper limit to the solar zenith angle for which our algorithm can reliably be applied. Unsatisfactory results will no doubt occur when the solar zenith angle $\theta_0 \gtrsim 80^\circ$, a switch that must be set in the operational code. In addition to reduced sensitivity for large solar zenith angles, there are additional complications arising from increased probability of shadows and finite and 3-dimensional cloud effects. This is a problem that exists with all such solar cloud reflectance algorithms, and we currently plan to set this $\theta_0^{\max} = 80^\circ$.

5. References

- Ackerman, S., K. Strabala, P. Menzel, R. Frey, C. Moeller, L. Gumley, B. Baum, C. Schaaf, G. Riggs and R. Welch, 1996: *Discriminating Clear-Sky from Cloud with MODIS Algorithm Theoretical Basis Document (MOD35)*. Algorithm Theoretical Basis Document ATBD-MOD-06, NASA Goddard Space Flight Center, 119 pp.
- Arking, A., 1964: Latitudinal distribution of cloud cover from TIROS III photographs. *Science*, **143**, 569–572.
- _____, and J. D. Childs, 1985: Retrieval of cloud cover parameters from multispectral satellite images. *J. Climate Appl. Meteor.*, **24**, 322–333.
- Bevington, P. R., 1969: *Data Reduction and Error Analysis for the Physical Sciences*. McGraw-Hill, 336 pp.
- Cess, R. D., G. L. Potter, J. P. Blanchet, G. J. Boer, S. J. Ghan, J. T. Kiehl, H. Le Treut, Z. X. Li, X. Z. Liang, J. F. B. Mitchell, J. J. Morcrette, D. A. Randall, M. R. Riches, E. Roeckner, U. Schlese, A. Slingo, K. E. Taylor, W. M. Washington, R. T. Wetherald and I. Yagai, 1989: Interpretation of cloud-climate feedback as produced by 14 atmospheric general circulation models. *Science*, **245**, 513–516.
- Cline, A. K., 1974: Scalar- and planar-valued curve fitting using splines under tension. *Comm. Assoc. Comput. Mach.*, **17**, 218–220.
- Curran, R. J., H. L. Kyle, L. R. Blaine, J. Smith and T. D. Clem, 1981: Multichannel scanning radiometer for remote sensing cloud physical parameters. *Rev. Sci. Instrum.*, **52**, 1546–1555.
- _____, and M. L. C. Wu, 1982: Skylab near-infrared observations of clouds indicating supercooled liquid water droplets. *J. Atmos. Sci.*, **39**, 635–647.
- Downing, H. D., and D. Williams, 1975: Optical constants of water in the infra-

red. *J. Geophys. Res.*, **80**, 1656–1661.

Durkee, P. A., 1989: Observations of aerosol-cloud interactions in satellite-detected visible and near-infrared radiance. *Proc. Symposium on the Role of Clouds in Atmospheric Chemistry and Global Climate*, American Meteorological Society, Anaheim, CA, 157–160.

Foot, J. S., 1988: Some observations of the optical properties of clouds. I: Strato-cumulus. *Quart. J. Roy. Meteor. Soc.*, **114**, 129–144.

Grainger, R. G., 1990: The calculation of cloud parameters from AVHRR data. *Ph.D. Dissertation*, University of Auckland, New Zealand, 188 pp.

Hale, G. M., and M. R. Querry, 1973: Optical constants of water in the 200-nm to 200- μ m wavelength region. *Appl. Opt.*, **12**, 555–563.

Han, Q., W. B. Rossow and A. A. Lacis, 1994: Near-global survey of effective droplet radius in liquid water clouds using ISCCP data. *J. Climate*, **7**, 465–497.

_____, W. Rossow, R. Welch, A. White and J. Chou, 1995: Validation of satellite retrievals of cloud microphysics and liquid water path using observations from FIRE. *J. Atmos. Sci.*, **52**, 4183–4195.

Hansen, J. E., and J. B. Pollack, 1970: Near-infrared light scattering by terrestrial clouds. *J. Atmos. Sci.*, **27**, 265–281.

_____, and L. D. Travis, 1974: Light scattering in planetary atmospheres. *Space Sci. Rev.*, **16**, 527–610.

Irvine, W., M., and J. B. Pollack, 1968: Infrared optical properties of water and ice spheres. *Icarus*, **8**, 324–360.

Kaufman, Y. J., and T. Nakajima, 1993: Effect of Amazon smoke on cloud microphysics and albedo. *J. Appl. Meteor.*, **32**, 729–744.

King, M. D., 1981: A method for determining the single scattering albedo of

- clouds through observation of the internal scattered radiation field. *J. Atmos. Sci.*, **38**, 2031–204.
- _____, 1987: Determination of the scaled optical thickness of clouds from reflected solar radiation measurements. *J. Atmos. Sci.*, **44**, 1734–1751.
- _____, L. F. Radke and P. V. Hobbs, 1990: Determination of the spectral absorption of solar radiation by marine stratocumulus clouds from airborne measurements within clouds. *J. Atmos. Sci.*, **47**, 894–907.
- _____, Y. J. Kaufman, W. P. Menzel and D. Tanré, 1992: Remote sensing of cloud, aerosol and water vapor properties from the Moderate Resolution Imaging Spectrometer (MODIS). *IEEE Trans. Geosci. Remote Sens.*, **30**, 2–27.
- _____, M. G. Strange, P. Leone and L. R. Blaine, 1986: Multiwavelength scanning radiometer for airborne measurements of scattered radiation within clouds. *J. Atmos. Oceanic Technol.*, **3**, 513–522.
- _____, W. P. Menzel, P. S. Grant, J. S. Myers, G. T. Arnold, S. E. Platnick, L. E. Gumley, S. C. Tsay, C. C. Moeller, M. Fitzgerald, K. S. Brown and F. G. Osterwisch, 1996: Airborne scanning spectrometer for remote sensing of cloud, aerosol, water vapor and surface properties. *J. Atmos. Oceanic Technol.*, **13**, 777–794.
- Kou, L, D. Labrie and P. Chylek, 1993: Refractive indices of water and ice in the 0.65- to 2.5- μm spectral range. *Appl. Opt.*, **32**, 3531–3540.
- Kratz, D. P., 1995: The correlated k-distribution technique as applied to the AVHRR channels. *J. Quant. Spectrosc. Radiat. Transfer*, **53**, 501–517.
- Menzel, W. P., and L. E. Gumley, 1996: *MODIS Atmospheric Profile Retrieval Algorithm Theoretical Basis Document*. ATBD-MOD-07, NASA Goddard Space Flight Center, 32 pp.
- _____, and K. Strabala, 1996: *Cloud Top Properties and Cloud Phase Algorithm Theo-*

retical Basis Document. ATBD-MOD-04, NASA Goddard Space Flight Center, 54 pp.

Mitchell, J. F. B., C. A. Senior and W. J. Ingram, 1989: CO₂ and climate: A missing feedback? *Nature*, **341**, 132–134.

Nakajima, T., and M. Tanaka, 1986: Matrix formulations for the transfer of solar radiation in a plane-parallel scattering atmosphere. *J. Quant. Spectrosc. Radiat. Transfer*, **35**, 13–21.

_____, and M. D. King, 1990: Determination of the optical thickness and effective particle radius of clouds from reflected solar radiation measurements. Part I: Theory. *J. Atmos. Sci.*, **47**, 1878–1893.

_____, and _____, 1992: Asymptotic theory for optically thick layers: Application to the discrete ordinates method. *Appl. Opt.*, **31**, 7669–7683.

_____, _____, J. D. Spinhirne and L. F. Radke, 1991: Determination of the optical thickness and effective particle radius of clouds from reflected solar radiation measurements. Part II: Marine stratocumulus observations. *J. Atmos. Sci.*, **48**, 728–750.

Nakajima, T. Y., and T. Nakajima, 1995: Wide-area determination of cloud microphysical properties from NOAA AVHRR measurements for FIRE and ASTEX regions. *J. Atmos. Sci.*, **52**, 4043–4059.

Ou, S. C., K. N. Liou, W. M. Gooch, and Y. Takano, 1993: Remote sensing of cirrus cloud parameters using Advanced Very High Resolution Radiometer 3.7 and 10.9 μm channels. *Appl. Opt.*, **32**, 2171–2180.

Palmer, K. F., and D. Williams, 1974: Optical properties of water in the near infrared. *J. Opt. Soc. Amer.*, **64**, 1107–1110.

Pilewskie, P., and S. Twomey, 1987: Cloud phase discrimination by reflectance measurements near 1.6 and 2.2 μm . *J. Atmos. Sci.*, **44**, 3419–3420.

- Platnick, S., 1991: Remote sensing the susceptibility of cloud albedo to changes in drop concentration. *Ph.D. Dissertation*, University of Arizona, Tucson, Arizona, 266 pp.
- _____, 1996: Impact of cloud inhomogeneity on the retrieval of cloud radiative and microphysical properties. *Proc. International Radiation Symposium*, Fairbanks, AK.
- _____, and S. Twomey, 1994: Determining the susceptibility of cloud albedo to changes in droplet concentration with the Advanced Very High Resolution Radiometer. *J. Appl. Meteor.*, **33**, 334–347.
- _____, and F. P. J. Valero, 1995: A validation study of a satellite cloud retrieval during ASTEX. *J. Atmos. Sci.*, **52**, 2985–3001.
- Ramanathan, V., 1987: The role of Earth radiation budget studies in climate and general circulation research. *J. Geophys. Res.*, **92**, 4075–4095.
- _____, E. J. Pitcher, R. C. Malone and M. L. Blackmon, 1983: The response of a spectral general circulation model to refinements in radiative processes. *J. Atmos. Sci.* **40**, 605–630.
- _____, R. D. Cess, E. F. Harrison, P. Minnis, B. R. Barkstrom, E. Ahmad and D. Hartmann, 1989: Cloud-radiative forcing and climate: Results from the Earth Radiation Budget Experiment. *Science*, **243**, 57–63.
- Rawlins, F., and J. S. Foot, 1990: Remotely sensed measurements of stratocumulus properties during FIRE using the C130 aircraft multichannel radiometer. *J. Atmos. Sci.*, **47**, 2488–2503.
- Revercomb, H. E., H. Buijs, H. B. Howell, D. D. LaPorte, W. L. Smith and L. A. Sromovsky, 1988: Radiometric calibration of IR Fourier transform spectrometers: Solution to a problem with the High-spectral resolution Interferometer Sounder. *Appl. Opt.*, **27**, 3210–3218.

- Robertson, C. W., and D. Williams, 1971: Lambert absorption coefficients of water in the infrared. *J. Opt. Soc. Amer.*, **61**, 1316–1320.
- Roeckner, E., U. Schlese, J. Biercamp and P. Loewe, 1987: Cloud optical depth feedbacks and climate modelling. *Nature*, **329**, 138–140.
- Rossow, W. B., F. Mosher, E. Kinsella, A. Arking, M. Despois, E. Harrison, P. Minnis, E. Ruprecht, G. Seze, C. Simmer and E. Smith, 1985: ISCCP cloud algorithm intercomparison. *J. Appl. Meteor.*, **24**, 877–903.
- _____, L. C. Gardner and A. A. Lacis, 1989: Global seasonal cloud variations from satellite radiance measurements. Part I: Sensitivity of analysis. *J. Climate*, vol. **2**, 419–458.
- Slingo, A., 1989: A GCM parameterization for the shortwave radiative properties of water clouds. *J. Atmos. Sci.*, **46**, 1419–1427.
- Spinhirne, J. D., R. Boers and W. D. Hart, 1989: Cloud top liquid water from lidar observations of marine stratocumulus. *J. Appl. Meteor.*, **28**, 81–90.
- Stamnes, K., S. C. Tsay, W. Wiscombe and K. Jayaweera, 1988: Numerically stable algorithm for discrete-ordinate-method radiative transfer in multiple scattering and emitting layered media. *Appl. Opt.*, **27**, 2502–2509.
- Stowe, L. L., H. Y. M. Yeh, , T. F. Eck, C. G. Wellemeyer, H. L. Kyle and the Nimbus-7 Cloud Data Processing Team, 1989: *J. Climate*, **2**, 671–709.
- _____, E. P. McClain, R. Carey, P. Pellegrino, G. Gutman, P. Davis, C. Long and S. Hart, 1991: Global distribution of cloud cover derived from NOAA/AVHRR operational satellite data. *Adv. Space Res.*, **11**, 51–54.
- Takano, Y., and K. N. Liou, 1989: Solar radiative transfer in cirrus clouds. Part I: Single-scattering and optical properties of hexagonal ice crystals. *J. Atmos. Sci.*, **46**, 3–19.
- _____, and _____, 1995: Radiative transfer in cirrus clouds. Part III: Light

- scattering by irregular ice crystals. *J. Atmos. Sci.*, **52**, 819–837.
- Tsay, S. C., K. Stamnes and K. Jayaweera, 1989: Radiative energy balance in the cloudy and hazy Arctic. *J. Atmos. Sci.*, **46**, 1002–1018.
- _____, _____ and _____, 1990: Radiative transfer in planetary atmospheres: Development and verification of a unified model. *J. Quant. Spectrosc. Radiat. Transfer*, **43**, 133–148.
- Twomey, S., and T. Cocks, 1982: Spectral reflectance of clouds in the near-infrared: Comparison of measurements and calculations. *J. Meteor. Soc. Japan*, **60**, 583–592.
- _____. and _____, 1989: Remote sensing of cloud parameters from spectral reflectance in the near-infrared. *Beitr. Phys. Atmos.*, **62**, 172–179.
- van de Hulst, H. C., 1974: The spherical albedo of a planet covered with a homogeneous cloud layer. *Astron. Astrophys.*, **35**, 209–214.
- _____, 1980: *Multiple Light Scattering: Tables, Formulas, and Applications*, Vols. 1, Academic Press, New York, 76–82.
- Vane, G., R. O. Green, T. G. Chrien, H. T. Enmark, E. G. Hansen, and W. M. Porter, 1993: The Airborne Visible/Infrared Imaging Spectrometer (AVIRIS). *Remote Sens. Environ.*, **44**, 127–143.
- Wang, M., and M. D. King, 1996: Rayleigh scattering effects on cloud optical thickness retrievals. *Proc. International Radiation Symposium*, Fairbanks, Alaska, *in press*.
- Wetherald, R. T., and S. Manabe, 1988: Cloud feedback processes in a general circulation model. *J. Atmos. Sci.*, **45**, 1397–1415.
- Wu, M. L. C., 1985: Quality of remote sensing measurements of cloud physical parameters in the Cooperative Convective Precipitation Experiment. *J. Geophys. Res.*, **90**, 10551–10562.

- Yang, P., and K. N. Liou, 1995: Light scattering by hexagonal ice crystals: Comparison of finite difference time domain and geometric optics models. *J. Opt. Soc. Am. A*, **12**, 162–176.
- _____. and _____, 1996a: Finite difference time domain method for light scattering by small ice crystals in three dimensional space. *J. Opt. Soc. Am. A* (in press).
- _____. and _____, 1996b: A geometric optics/integral-equation method for light scattering by nonspherical ice crystals. *Appl. Opt.* (in press).